

A HYBRID HYDRODYNAMIC-MONTE CARLO SIMULATION OF THE TRANSPORT  
OF NEUTRAL RADICALS IN LOW PRESSURE REMOTE PLASMA SOURCES

BY

MICHAEL JOSEPH HARTIG

B.S., University of Illinois, 1986

M.S., University of Illinois, 1989

THESIS

Submitted in partial fulfillment of the requirements  
for the degree of Doctor of Philosophy in Electrical Engineering  
in the Graduate College of the  
University of Illinois at Urbana-Champaign, 1992

Urbana, Illinois

A HYBRID HYDRODYNAMIC-MONTE CARLO SIMULATION OF THE TRANSPORT  
OF NEUTRAL RADICALS IN LOW PRESSURE REMOTE PLASMA SOURCES

Michael Joseph Hartig, Ph.D.  
Department of Electrical and Computer Engineering  
University of Illinois at Urbana-Champaign, 1992  
M. Kushner, Advisor

In low pressure electron cyclotron resonance and remote plasma enhanced chemical vapor deposition reactors (milliTorr to hundreds of milliTorr) the mean free path of excited state neutrals can be commensurate with the vessel dimensions. Deposition species may collide with the wall several times before encountering the substrate. While the movement of these particles is essentially ballistic, the advective flow of the background gas is a significant factor in the determination of the transport of the neutral radicals. To address these conditions, a hybrid hydrodynamic-Monte Carlo model has been developed. The advective flow field is calculated from the mass and momentum equations. Radical transport is then simulated using Monte Carlo techniques that include inelastic collisions with the background species and other MC particles, absorbing or reflective collisions with reactor surfaces, or momentum transfer with the advective fluid.

Presented here are the results describing the effects of geometry, pressure and gas flow for gas mixtures containing  $\text{SiH}_4$ . Identity, uniformity, and angle of incidence of the radical flux to the substrate will be addressed with the goal of optimizing the fluxes of selected species.

## ACKNOWLEDGMENTS

As with most people, it is difficult to properly thank all of the people who have helped me throughout the years. To simply cite the names of friends and family in the foreward of a thesis seems paltry compared to their help and understanding. I just want to let all of those mentioned here know that with these words go deep feelings of gratitude. I am truly fortunate to have known these people, even for a short time.

I wish to first thank my parents, Bob and Geraldine Reichel, and my sisters, Michele Ashe and Denise Dimer, for their caring and their love. Without their support and understanding, I could not have achieved a fraction of what I have done.

I wish to also thank my advisor, Professor Mark Kushner, for the time and effort that he put in to help me achieve the doctorate. Even though we did not always agree on things, I have come to sincerely respect his words and deeds. I have learned a great deal while working under his guidance and am greatly appreciative.

As for friends and coworkers, I have seen many come and go in my stay. They were the ones who helped me to keep a sense of myself in the chaos of graduate school. Those that stand out are: Laureen Fey, Fred Huang, Dori Thomas, Helen Hwang, Mike McCaughey, Rich Fraser, Tim Peck, Tim Sommerer, Jim Schloss, Kevin King, Emily Cheng, Laura Wozniak, Deanna Terven, Becky White, the gang in the Sung Lee Tae Kwon Do club, Jim and Pam Armstrong, the ODP and Gas House gang, and others who are too numerous to mention. Thank you one and all.

## TABLE OF CONTENTS

	Page
I. INTRODUCTION.....	1
II. DESCRIPTION OF MODEL.....	5
A. FLUID MODEL.....	6
B. MONTE CARLO MODEL.....	7
C. SIMULATION PARAMETERS.....	13
III. RESULTS.....	15
IV. DISCUSSION.....	22
V. CONCLUSIONS.....	26
TABLES.....	27
FIGURES.....	30
REFERENCES.....	51
VITA.....	56

## I. INTRODUCTION

The need for smaller device sizes in the semiconductor industry requires innovative approaches to semiconductor processing. Plasma processing methods are one such tool being used to achieve the critical specifications required in present day microelectronic devices. The use of remote plasma-enhanced chemical vapor deposition (RPECVD) has allowed the growth of epitaxial films on substrates at increasingly lower temperatures ( $< 500$  C).<sup>1-3</sup> The cleaning of silicon wafers can be accomplished in situ through the use of remote hydrogen plasmas<sup>4-5</sup> or electron cyclotron resonance (ECR) plasmas,<sup>6-7</sup> thus minimizing the contamination of the substrate. The etching of silicon and silicon oxide can be accomplished at lower pressures using ECR type plasmas or magnetically enhanced reactive ion etching. At these pressures, typically in the milli Torr to tens of milli Torr range, the reactive species and ions, in particular, experience few collisions before encountering the wafer, leading to near normal incidence on the substrate and a more anisotropic etch. In low-pressure deposition systems, the lack of collisions allows highly reactive radical species created in the plasma to reach the substrate while removing the substrate from the plasma. In low-pressure deposition systems, high plasma densities are required for high deposition rates.<sup>8</sup>

A complete understanding of the processes that lead to deposition or etching in plasma-assisted reactors is hindered by the complexity of the reaction schemes involved and the variety of excitation methods. For example, in remote PECVD, the substrate is placed outside the plasma zone. Whether the system is indirect RPECVD, in which generation of the deposition species is accomplished by exciting a carrier gas upstream in the plasma, or an intermediate system that uses a plasma to excite the deposition species directly, there is little known about the transport and deposition

process.<sup>9,10</sup> In low-pressure remote plasma systems, generation and transport effects dominate the characteristics of the radical flux to the substrate surface as opposed to gas phase chemistry.<sup>11</sup> As a result, there has been much research devoted to the transport mechanisms for various remote plasma deposition and etching reactors. The recent development of indirect RPECVD systems by Lucovsky, Tsu et al.<sup>12-19</sup> and others,<sup>3,20-25</sup> and experimental studies of ECR deposition systems<sup>26-34</sup> have resulted in many insights into the reaction channels and transport effects for a variety of pressures ( $10^{-4}$  to  $3 \times 10^{-3}$  Torr), and flow rates (0.5 - 250 sccm). The difficulties involved in observing certain radical species coupled with the vast parameter space for each system have left many questions about transport unanswered.

To address these questions, various theoretical and numerical studies have been developed to describe the radical generation, transport, and substrate deposition for plasma processing reactors. In the higher pressure regime ( $\geq 100$  mTorr), Chen<sup>35</sup> and Gallagher<sup>36</sup> solved the rate equations for reactions and transport, to determine the radical densities in silane plasmas. Chen calculated the deposition rate in a flowing CVD reactor as a function of precursor gas concentration, diffusion constant, and reactor vessel radius. Gallagher showed that in a PECVD reactor using silane, the dissociation product  $\text{SiH}_3$  produces 98% of the deposited Si on the substrate. Tachibana<sup>37</sup> included ion species in a comprehensive model to show that  $\text{SiH}_3$  is the dominant radical found in a PECVD reactor using  $\text{SiH}_4$ . Yamaguchi et al.<sup>38</sup> solved Poisson's equation in a one-dimensional solution to the silane system to determine the spatial distribution of radical species in a PECVD reactor. Kushner<sup>45</sup> recently solved for the densities of excited state species in a two-dimensional model of an indirect RPECVD reactor. He used excitation transfer from metastable and ion states of a rare gas buffer to optimize the

radical flux to the substrate. Other fluid calculations have been performed on systems containing various gas mixtures.<sup>39-41</sup>

Fluid models often fail at low-pressures when solving for the electron densities, where the mean free path becomes commensurate with the size of the vessel. Koch and Hitchon<sup>42</sup> used a kinetic model self-consistently with the electric field to track the electron and ion densities and the electron distribution function in a silane glow discharge. Garscadden,<sup>43</sup> Kushner,<sup>44-45</sup> Sato and Tagashira,<sup>46</sup> and Sommerer and Kushner,<sup>47</sup> have incorporated Monte Carlo methods to solve for electron densities and impact rate coefficients in RF discharges while using a hydrodynamic method to solve for heavy particle parameters. At very low-pressures, Porteous and Graves<sup>48</sup> have determined ion densities and transport using Monte Carlo techniques while modeling the electrons using a fluid scheme. Similar hybrid methods that solve for equilibrium species using fluid methods and solve for nonequilibrium species parameters via Monte Carlo techniques have been used to model the "hot" kinetics of F atoms in  $\text{CF}_4$  etching plasmas.<sup>49</sup>

While modeling heavy particles using the hydrodynamic equations is adequate for the pressures  $\geq 100$  mTorr, at lower pressures the mean free path of low-density radical species can be centimeters, which is on the order of the reactor dimensions. Thus, the radical species do not necessarily come into equilibrium with the background gas. For example, at a pressure of 10 mTorr, and assuming a momentum transfer cross section,  $\sigma$ , of  $5 \text{ \AA}^2$ , the mean free path  $\lambda = (N\sigma)^{-1} = 6 \text{ cm}$ . Therefore, the use of ensemble parameters to describe the transport of these radicals is inaccurate. Monte Carlo techniques are then called for to describe the ballistic nature of radical species at these pressures.<sup>19</sup> However, for gas pressures from 1 mTorr to hundreds of mTorr, the efficiency of Monte Carlo methods to account for all gas species densities and

velocities is limited by the larger densities of the ground state gas species which dominate the calculation.

A hybrid model is presented here that utilizes a fluid model for the background gas and solves for the advective flow field. The radical species transport is modeled using Monte Carlo techniques. Elastic collisions with the background gas by the Monte Carlo particles are calculated, and momentum transfer is determined by the advective flow field. Inelastic collisions of the Monte Carlo particles with the background gas and other MC particles are considered, as well as collisions with the reactor surfaces. In Chapter II, a detailed description of the model is given together with reaction data and sticking coefficients. Chapter III describes the results obtained for application of the model to an argon/silane system. A discussion of the results is found in Chapter IV with concluding remarks presented in Chapter V.



## II. DESCRIPTION OF MODEL

The model is divided into two parts. The first part, the fluid model, considers the background flowing gas as a continuous fluid. The continuity equations of mass and momentum are used to describe the advection and diffusion of the gas mixture. Boundary conditions are applied and the hydrodynamic differential equations are integrated in time to solve for the mass and momentum densities on a two-dimensional grid within the reactor. The second part, the particle or Monte Carlo model, addresses the excited state species produced in the reactor. Particles representing neutral excited state radicals produced in the plasma are introduced with a given velocity, and are allowed to transport. The trajectories are integrated over time, with statistics taken of the particle's identity, weight, and position after each time step, with the results transferred to the grid used in the fluid model. All collisions, both elastic and inelastic, are accounted for by interactions with the densities recorded in the grid array. This allows for momentum transfer with the background gas as well as chemical reactions with other excited state species.

The model addresses a cylindrically symmetric low-pressure reactor schematically shown in Fig. 1. The pressure range of interest is 1 mTorr to 25 mTorr, which is similar to values found in low-pressure deposition or etching systems. The system is divided into the two regions, the plasma region and the deposition region. The neutral radical species are created in the plasma region. The substrate is located on the axis in the deposition region, separated from the vessel walls by the exit port. The regions are concentric, with the radius of the plasma region less than the radius of the deposition region. Gas enters the chamber through the plasma region and flows downstream. The gas exits through a port located around the edges of the wafer. The

reactor dimensions, surface and gas temperature, and flow rates are input parameters to the model.

#### A. FLUID MODEL

The fluid model addresses the higher density background gas which flows into the reactor. The differential equations for mass and momentum conservation are solved on a two-dimensional, cylindrically symmetrical grid. The solution consists of an integration in time until the values converge to a steady state. The final mass and momentum densities are later used in the Monte Carlo model.

Calculation of the advective field is necessary to accurately model elastic collisions of the radical species with the background gas which result in momentum transfer. At the pressures considered, a full accounting of the advective flow field involves the calculation of laminar and turbulent flow fields. Such a model is both complicated and costly.<sup>50</sup> The flow of the background gas is thus simplified by the approximation of a purely advecting, compressible fluid, and a general flow field is found using a continuum description of the background gas.

As stated above, the advective flow field is calculated by solving the continuity equations for mass and momentum. For mass conservation, the equation is

$$\frac{dN_i}{dt} = - \nabla \cdot (N_i \mathbf{v} - D_i \nabla N_i) \quad (1)$$

where  $N_i$  and  $D_i$  are the density and diffusion coefficients for species  $i$ , respectively, and  $\mathbf{v}$  is the species velocity. Momentum conservation is described by

$$\frac{d(\rho \mathbf{v})}{dt} = - \nabla \cdot \rho \mathbf{v} \mathbf{v} - \nabla P = - \nabla \cdot \rho \mathbf{v} \mathbf{v} - \nabla (NkT) \quad (2)$$

where  $\rho$  is the mass density of the gas,  $P$  is the pressure,  $N$  is the total gas

density,  $T$  is the gas temperature, and  $k$  is Boltzmann's constant. The boundary conditions are

$$N_i v = \text{constant} \quad (3)$$

at the inlet and output ports,  $z = 0$  and  $L$ , respectively;

$$vN = 0 \quad (4)$$

at  $z = 0, L$ , and  $r = 0, R$ ; and finally

$$\rho v = 0 \quad (5)$$

at  $r = 0, R$ . The pressures are low enough so that any heating in the plasma zone that may occur is convected to the wall quickly enough. Gas heating is therefore not a significant process. The gas is assumed isothermal and set to the wall temperature.

To arrive at a stable solution, the time steps in the integration of the equations are chosen to be 0.1 to 0.25 of the Courant limit. The equations are written using the donor cell method. Mass and momentum derivatives are calculated based on the flux into and out of each grid cell. The derivatives are then integrated using a third-order Runge-Kutta method until the solution converges to steady-state values. An example of the resulting advective flow field is given in Fig. 2.

## B. MONTE CARLO MODEL

The transport of the excited state neutral and radical species is determined using a Monte Carlo technique. Particles are created and launched in the plasma zone. The particles represent one of the neutral radical species and are assigned a weighting corresponding to the number of atoms the particle represents. An initial velocity for that particle is also assigned. After freely moving along its trajectory for a randomly chosen time period, the particle undergoes a "collision" with another particle of the ground or excited state or radical species. The species the particle collides with and

the type of collision that takes place are randomly chosen from a distribution weighted by the rate coefficients for each collision. For an inelastic collision, momentum is exchanged with the flowing background gas. If the collision is inelastic, the species identity of the particle is changed accordingly and a new velocity is assigned to the particle. New particles are introduced if the collision chosen is a chemical reaction which produces two different types of species.

Particles that encounter a surface are placed at the point of contact. A random number is chosen and compared to a sticking coefficient to determine if the particle is "adsorbed" and no longer considered, or "reflected" and given a new velocity. After each time step for the particle, statistics are taken on the particle densities onto the grid used in the fluid model. The density is recorded using the species type, weighting of the particle, the time spent in the cell during the last time step, and the volume of the cell. This gives a continuous update for the density of various radical species throughout the reactor. Similar statistics are taken for particles that are adsorbed or react on the substrate.

The simulation begins with the reactor void of any Monte Carlo particles. Neutral radical species are introduced into the simulation in the plasma zone and continue to be created until the system reaches a steady state. Introduction of plasma created particles is done on a quasi-continuous basis by the random placement of particles in the plasma zone. This zone is a subvolume located within the plasma region and has boundaries that are input parameters. The choice of position is radially weighted in the form

$$R_{\text{pos}} = [r(R_{\text{out}}^2 - R_{\text{in}}^2) + R_{\text{in}}^2] \quad (6)$$

where  $R_{\text{pos}}$  is the initial radial position of the particle chosen,  $R_{\text{out}}$  and  $R_{\text{in}}$  are the outer and inner radial positions of the plasma zone, respectively, and  $r$  is a uniformly distributed random number chosen on (0,1). The particles are

either given an initial energy determined from a Maxwellian distribution which has its average energy the gas temperature, or are introduced "hot," that is, they are introduced with an initial velocity greater than the gas temperature. This excess energy reflects the energy difference between the dissociative state of the parent molecule and the ground state of the fragments. See Ref. 49 for further discussion of this effect.

The probability that the time between collisions for a given particle is in the interval  $t$  and  $(t + dt)$  is<sup>51</sup>

$$P(t)dt = \nu \exp(-\nu t) \quad (7)$$

where  $\nu$  is the total collision frequency. Integration of Eq. (7) from 0 to  $\Delta t$  yields the cumulative distribution function. The limits of this function are 0 and 1 for  $\Delta t = 0$  to  $\infty$ , and therefore can be equated to a random number,  $r$ , from a uniform distribution. The subsequent inversion of the integrated equation results in a randomly chosen collision time,

$$\Delta t = \frac{1}{\nu} \ln(r) . \quad (8)$$

The collision frequency for species  $i$ ,  $\nu_i$ , is calculated from the sum of the rate coefficients for collisions that species  $i$  can have with other species  $j$ ,  $k_{ij}$  multiplied by the density of the collision partner,  $N_j$ ,

$$\nu_i = \sum_j N_j k_{ij} \quad (9)$$

which is calculated before the simulation begins. For the collisions with the background gas species, the densities of the collision partners are known. However, if the collision partner is a MC species, i.e., another neutral radical, then the density used in Eq. (9) is an estimate of the maximum density for that species. If during the simulation the collision chosen is one in which the reaction partner is another Monte Carlo particle, the density array which has recorded the latest values of density for the reaction partner is examined for the mesh location which the particle occupies. A random number

is chosen and compared to the ratio of the actual present density divided by the estimated maximum value. If  $r \leq N(r,z)/N_0$ , then a collision occurs. If not, the collision is a "null" collision, and the particle is allowed to continue on its trajectory.<sup>52</sup>

During the update of a particle trajectory, its initial and final positions are checked. If the particle's final position takes it outside the boundaries of the vessel, or if the combination of initial and final positions can be arrived at only by traveling through the vessel walls such as at an inside corner, then the particle is placed at the point of contact with the wall and its individual time is updated accordingly. Otherwise, the particle is left at its final position. After the particle's position is updated, its location is determined in relation to the grid used from the fluid model. The density of that species is then integrated within the fluid mesh commensurate with the time the particle has spent in that mesh location. At any given time, the density for a given mesh location,  $k$ , and given species,  $i$ , is

$$N_i = \frac{1}{\Delta T} \sum_j \frac{W_j}{V_k} \Delta t_j \quad (10)$$

where the sum is over all particles crossing through the cell;  $W_j$  is the weight of the  $j$ th particle occupying that cell,  $V_k$  is the volume of the cell,  $\Delta t_j$  is the time the  $j$ th particle has spent within the cell, and  $\Delta T$  is the total time of the simulation.

At the end of the free path, the particle undergoes a collision. The collision chosen is selected from a list of reactions input to the model at the start of the simulation. A given radical species may undergo either "elastic" collisions with the background gas, or "inelastic" chemical reactions with background gas or excited state species. Before the simulation begins, the probability for each collision that a species may experience is calculated at every mesh cell by using the input rate coefficient multiplied

by the density of the collision partner, and normalized to the total collision rate for that species and cell. This gives a weighted distribution for the collisions that the particle may undergo. The choice of the type of collision can be accomplished by choosing a random number and comparing that number to the distribution.

At pressures  $\geq 1$  mTorr, the transport of neutral radicals and excited state species can be significantly affected by momentum transfer collisions with the background gas. This process can be efficiently modeled by using "elastic" collisions which couple the transport of the Monte Carlo particles to the fluid. Since the algorithm for collisions of the Monte Carlo particles with other species uses the fluid mesh to account for densities, it is straightforward to account for momentum transfer with the fluid in a similar fashion. In this way, all collisions can be treated in a general "non-selective" fashion. Consider an "elastic" collision of the form:  $A + M \rightarrow A + M$ , where  $A$  is the incoming particle and  $M$  is a background gas species. To determine the momentum transfer to  $A$ , the total fluid momentum density of that cell is used for  $M$ . Transfer of momentum is performed by first transforming the coordinate system to that of the advecting fluid. The velocity of the particle after the collision,  $V_{\text{new}}$ , is obtained from<sup>53</sup>

$$V_{\text{new}}^2 = V_{\text{old}}^2 \left[ 1 - \frac{2mM}{(m+M)^2} (1 - \cos(\Gamma)) \right], \quad (11)$$

where  $V_{\text{old}}$  is the transformed velocity of the Monte Carlo particle before the collision,  $m$  is the mass of the Monte Carlo particle,  $M$  is the mass of the collision partner, and  $\Gamma$  is the scattering angle of the Monte Carlo particle. The angle  $\Gamma$  randomly chosen from an isotropic distribution.

A deficiency in this exchange of momentum is that the Monte Carlo

particle eventually loses all thermal motion as it "thermalizes" with the advectively flowing background gas. Since the flow field addresses the ensemble motion of the background gas and does not allow for random thermal motion, the particles begin to pool in areas where the background gas becomes stagnant. To account for the thermal component of the background fluid during a particle-fluid collision, a randomly selected thermal velocity is added to the advective velocity of the fluid element. In practice, a fraction of the full gas temperature is used for this velocity, typically 0.5. The velocity of the Monte Carlo particle is then converted back to the laboratory coordinate system. The particle is given a new free time before collision, and allowed to continue along its new trajectory. The effect of adding a thermal component to the fluid element is addressed in Chapter IV.

If the collision is "inelastic" or chemical ( $A + B \rightarrow C$ ), then the particle adopts a new identity or is rendered inactive, depending on whether species C is a Monte Carlo species warranting further tracking. New particles are introduced for reactions of the form  $A + B \rightarrow C + D$ , where species D is another Monte Carlo species.

If the particle hits a wall or the substrate, then another random number is chosen and compared to the sticking coefficient for that surface. Random numbers that are less than the sticking coefficient result in the particle sticking to the surface, and the particle is removed from the simulation; otherwise, the particle is given a new velocity with a kinetic energy chosen from a Gaussian distribution peaked at the surface temperature and a direction chosen from a Lambertian distribution to make the reflection of the particle diffusive.

The locations of particles that hit the substrate are recorded, based on the fluid model grid. The mesh cell on the substrate where the particle hits is calculated, and the particle's identity and weight are noted and integrated



into the total flux of particles to the surface. Flux profiles of particles hitting and sticking on the substrate are then obtained. Angles of incidence are recorded for all particles and averaged later to calculate the average angle of incidence versus radial position on the substrate. Those particles which pass through the inlet or output ports are removed from the simulation.

### C. SIMULATION PARAMETERS

The dimensions of the reactors investigated were similar to those of the typical low-pressure reactors described above. The length of the plasma region is kept constant at 20 cm, and the radius of the deposition region is set at 14 cm. The gas mixture is  $\text{Ar/SiH}_4 = 95/5$ . The gas flow rate is 100 sccm. The gas and wall temperatures are 300 K, while the substrate temperature is 523 K. The width of the plasma region is varied between 3 cm and 13 cm while the plasma is 0.5 cm less in radius than the region. The length of the deposition region is varied between 10 cm and 30 cm. The substrate radius is varied between 6 cm and 11 cm. The pressures investigated run from 1 mTorr to 25 mTorr.

The diffusion coefficients used in the hydrodynamic calculation of the advective flow field were calculated from Hirschfelder et al.,<sup>54</sup> with Lennard-Jones parameters taken from Ref. 44. The parameters for  $\text{SiH}_4$  and Ar are listed together with those of the Monte Carlo species in Table 1. The excited state neutral species and radicals which were tracked as Monte Carlo particles are also given in Table 1. Those species created in the plasma zone are designated with a dagger. Early investigations revealed that atomic Si was not produced in a large enough quantity to warrant consideration as a Monte Carlo particle. The heavier silicon containing polymers were also neglected as Monte Carlo particles since the production of these species from  $\text{SiH}_4$  requires several intermediate collisions, and, at the pressures being considered, the

likelihood that any individual particle would have enough collisions to create such polymers is unlikely.

Atomic hydrogen is included in the model as two separate Monte Carlo species: those that are created as the dissociation product of  $\text{SiH}_4$  yielding  $\text{SiH}_3$  and  $\text{H}$ , and those created as the dissociation product giving  $\text{SiH}_2$  and  $2\text{H}$ . From momentum conservation, dissociation to  $\text{SiH}_2$  and to  $\text{SiH}_3$  yields hydrogen atoms with different energies. Therefore, by treating each hydrogen as a separate species, the correct velocities can then be assigned.

The list of reactions for the neutral radicals in the Monte Carlo model is given in Table 2. The rate coefficients listed are taken from various sources<sup>55-68</sup> and are referenced accordingly. Momentum transfer reactions are designated as  $\text{X} + \text{M} \rightarrow \text{X} + \text{M}$  where  $\text{X}$  is the radical species and  $\text{M}$  is the background gas species with a density equal to the total background gas density. The rate coefficients for elastic collisions are recalculated from the Lennard-Jones parameter,  $\sigma$ , using the expression

$$k = v_{\text{th}} \pi \sigma^2 \quad (12)$$

where  $v_{\text{th}}$  is the average thermal velocity given by

$$v_{\text{th}} = \left[ \frac{8\pi KT}{\text{M}} \right]^{\frac{1}{2}} \quad (13)$$

where  $T$  is the gas temperature,  $\text{M}$  is the mass of the radical species, and  $K$  is Boltzmann's constant. The Lennard-Jones parameters are the same as those used by Kushner<sup>44</sup> where he assumed values similar to those of methane counterparts, when available, and estimated values, otherwise. Sticking coefficients for the different species on the wall and substrate were obtained from Perrin and Broekhuizen<sup>69</sup> and Kushner,<sup>45</sup> with values estimated for radical species not listed in these references. Since it is difficult to obtain a consistent value for the measured sticking coefficient for the neutral radicals,<sup>70</sup> the values listed are considered approximate.

## III. RESULTS

One of the unique features of the model described is the ability to efficiently model the background flowing gas and account for the interaction of the excited state species with the advective flow field. The effect of the advective field on the density of  $\text{SiH}_3$  at 25 mTorr is shown in Fig. 3. The solid contours are the density obtained considering momentum transfer with the flow field, while the broken lines are the density found when the background gas is stagnant. The radical  $\text{SiH}_3$  is predominantly created in the plasma region, between  $z = 2.5$  cm and 12.5 cm. In both cases, all radicals are created in the plasma region at the background gas temperature to avoid hot atom effects. In the plasma region in which the  $\text{SiH}_3$  is predominantly created, the particles have had relatively few momentum transfer collisions with the background gas but have many collisions with the walls. The average downstream velocity of the particles in this volume is therefore small. As the particles move downstream, they continue to have more collisions with the advecting background gas and gain more average downstream velocity from the additional momentum transferred. The effect is cumulative, resulting in a larger downstream shift of the contours in the deposition region in comparison to the plasma region. The fluxes of  $\text{SiH}_3$  particles to the substrate for these cases are shown in Fig. 4 for pressures of 1 mTorr and 25 mTorr. At both pressures, a rise in the flux of radicals to the substrate for the advecting gas is found. Since the total flow rate is the same in both cases, then  $Nv$  is a constant. The collision frequency scales as  $N$ , and momentum transfer scales as  $v$ . Therefore, in spite of the lower pressure, the effect of the flow field is nearly the same. In a stagnant background gas, the smaller velocity of the radicals downstream allows the  $\text{SiH}_3$  particles to collide with the walls of the vessel more often. This results in decreasing the density of radicals that

actually make it to the substrate. They are, instead, lost at walls where they recombine with atomic hydrogen to return to the ground state gas species.

The pressure dependence of  $\text{SiH}_3$  density in a flowing field is shown in Fig. 5. Radical species are created hot in the plasma zone, with an energy of 2 eV. The generation rate of radicals in the plasma is inversely proportional to pressure so as to make a proper comparison between the different pressures. The  $\text{SiH}_3$  density has a smaller gradient downstream for the 1 mTorr case when compared to the 10 mTorr and 25 mTorr cases. At the higher background gas densities, the increased collision frequency tends to reduce the free transport of the  $\text{SiH}_3$  downstream. The increased scattering effectively reduces the axial component of the average drift velocity. While the  $\text{SiH}_3$  is nearly nonreactive with other gas species, the slower axial velocity allows for more collisions with the walls, resulting in a reduced density from wall losses. Rossnagel<sup>71</sup> observed experimentally that as pressure increases, the increase in gas scattering of sputtered atoms from the cathode leads to redeposition of the sputtered atoms back onto the cathode and a reduction in deposition on the anode. In a similar fashion, increases in gas scattering of the  $\text{SiH}_3$  particles allow for more wall losses, reducing the number of particles that reach the substrate.

The average angle from normal incidence for all deposition species is shown in Fig. 6 for different pressures. The deposition region length in each case is 30 cm. At 1 mTorr, the particles hit the substrate at a minimum average angle of 22 - 23 deg. This average angle rises across the substrate to 28 - 29 deg at the edge of the substrate. The angle of incidence becomes more uniform across the substrate as the pressure increases, whereas the mean value increases slightly with rising pressure. The uniform rise of the incidence angle values is indicative of a higher frequency of collisional scattering of the radical species before being deposited on the substrate. The variation of

incidence angle across the substrate, seen predominantly at lower pressures, is caused by hot atom effects, which will be addressed below.

As the pressure rises, chemical reactions with the background species become significant. The density of  $\text{Ar}^*$  is shown in Fig. 7 for 1 mTorr and 25 mTorr. The rate of quenching of metastable argon becomes significant at 25 mTorr resulting in a larger gradient of  $\text{Ar}^*$  density from the plasma source. The loss rate is much smaller at pressures of 1 mTorr and below, allowing a significant flux of  $\text{Ar}^*$  to reach the substrate before being quenched.

Losses from chemical reactions can have a significant effect on the deposition radicals. The density for  $\text{SiH}_2$  at 1 mTorr and 25 mTorr is shown in Fig. 8. The chemical reaction of the  $\text{SiH}_2$  with silane to produce  $\text{Si}_2\text{H}_6$  becomes comparable to wall losses at 25 mTorr, resulting in the larger density gradients. This effect can be seen in Fig. 9, which shows the ratio of flux vs. radius of  $\text{SiH}_2$  to the flux of  $\text{SiH}_3$ , at the pressures and geometries used in Figs. 5 and 8. At 25 mTorr, the density of  $\text{SiH}_2$  is depleted from chemical reactions so that the flux of  $\text{SiH}_2$  to the substrate is only 10% of the flux of  $\text{SiH}_3$ . However, at 1 mTorr, the flux of  $\text{SiH}_2$  becomes comparable to that of  $\text{SiH}_3$ . The slight dip at the center of the substrate in the ratio for the 1 mTorr case is attributable to hot atom effects, which will now be discussed.

Figures 10(a) and (b) shows the density of  $\text{SiH}_3$  during the rise to steady state, at pressures of 1 mTorr and 10 mTorr, respectively. The 1 mTorr case is shown at a time of 0.3 ms after the plasma is turned on, and the 10 mTorr case is at 3 ms, both reflecting similar fractions of residence time for the particles in the vessel. For the 1 mTorr case, the density peaks near the substrate, while the density for the 10 mTorr case remains small. This is due to hydrogen atoms which are created hot in the plasma region. At lower pressures, they travel ballistically to the substrate, experiencing few collisions along the way. Once in contact with the substrate, they lose much

of their energy, coming off of the substrate at energies equivalent to the substrate temperature. At the lower velocities, the hydrogen atoms remain in the region near the substrate long enough to undergo extraction reactions with the surrounding silane to form  $\text{SiH}_3$  and  $\text{H}_2$ , leading to the observed rise in density. At 10 mTorr, the atoms produced in the plasma region see more collisions during transport to the substrate, allowing most of the atoms to thermalize before reaching the substrate. The density for hydrogen atoms created from the dissociation of  $\text{SiH}_4$  to create  $\text{SiH}_2$  is shown in Fig. 11(a), and the density of hydrogen atoms created from the dissociation of  $\text{SiH}_4$  to create  $\text{SiH}_3$  is shown in Fig. 11(b). The hydrogen created with  $\text{SiH}_3$  has greater initial speeds than the atoms produced with  $\text{SiH}_2$  due to momentum conservation. The density contours in Fig. 11(b) reveal larger densities at the substrate of H atoms created with  $\text{SiH}_3$  than those created with  $\text{SiH}_2$ . The difference comes about from the higher velocity H atoms ballistically transporting to the substrate surface, cooling upon contact with the surface, and pooling in the region around the center of the substrate. This larger density of hydrogen is then the source for the extraction reaction described above producing higher densities of  $\text{SiH}_3$  near the center of the substrate.

As mentioned above, the effect of the ballistic hydrogen atoms is revealed in the smaller average angle of incidence at lower pressures observed in Fig. 6. Although only 10% of the hydrogen atoms that hit the substrate reacts, the ballistically transported hydrogen flux is high enough to give a more perpendicular average incidence angle at the center of the substrate. The higher densities of  $\text{SiH}_3$  seen at the center will then drive the ratio of  $\text{SiH}_2/\text{SiH}_3$  down in this vicinity, as was mentioned above for Fig. 9. These effects are not seen at higher pressures, where the incidence of ballistic hydrogen atoms is much smaller.

To quantify the effect of these hot atoms on the flux of deposition

species to the substrate, a simulation was performed in which the radicals were created at the gas temperature. The reactor deposition region is 30 cm long. The plasma region is 6 cm in radius. Figure 12 shows the ratio of  $\text{SiH}_3$  flux for radicals created hot with respect to the flux calculated for radicals created cool. The results are shown for various pressures. While the 25 mTorr case shows only a slight enhancement of the  $\text{SiH}_3$  along the radius, the 1 mTorr case reveals enhancements of up to 35% at the center of the substrate, with the effect being smaller at the edge. Enhancements of approximately 10% can be observed at the center of the substrate for the 10 mTorr case. The radial dependence of enhancement of  $\text{SiH}_3$  flux at lower pressures due to hot atoms is thus one factor leading to the nonuniformity of film growth on the substrate.

The model was modified to allow the generation of the neutral radicals in the plasma at the gas temperature rather than at higher energies to see the effect of the hot atoms on the average angle of incidence. Figures 13(a) and (b) show the results at pressures of 1 mTorr and 25 mTorr, respectively. The cases in which the  $\text{SiH}_2$ ,  $\text{SiH}_3$ , and H are created hot produce results in which the average incidence angle at the center of the substrate is more perpendicular than in the cases in which they are generated at the gas temperature. The effect is lessened at the edge of the substrate. The fractional change is diminished slightly at the higher pressure where the maximum change is of  $\sim 10\%$  for the 1 mTorr case as opposed to  $\sim 7\%$  at 25 mTorr.

The effect of geometry on deposition flux and incidence angle is a major concern. The densities of  $\text{SiH}_3$  at 1 mTorr for various radii of the plasma region are shown in Fig. 14. Compared with Fig. 5(a), which shows the density found for a plasma region of 6 cm, there are larger density gradients of the  $\text{SiH}_3$  along the axis as the plasma region radius becomes smaller. The ratio of wall area around the plasma region to port area leading to the deposition

region is much larger at smaller radii. The  $\text{SiH}_3$  encounter the walls of the reactor more frequently. Since loss to the wall is the dominant loss channel for the  $\text{SiH}_3$ , the higher density gradient is expected.

Wall loss effects are more readily apparent for more reactive species. Figure 15 shows the density for the excited state of argon at radii of 3 cm, 6 cm, and 10 cm. Again, at smaller radii, the argon metastable state is quenched before leaving the plasma region due to frequent loss at the vessel walls. As the plasma region radius increases, significant densities of  $\text{Ar}^*$  escape the plasma region and are able reach the substrate. This can be seen in Fig. 15(b) for a plasma region radius of 6 cm. This fraction continues to increase at even larger radii as can be seen in Fig. 15(c) for a radius of 10 cm. The density of  $\text{Ar}^*$  at 25 mTorr for various plasma region radii is shown in Fig. 16. In these cases,  $\text{Ar}^*$  is the only excited state generated, which accounts for the higher maximum density seen when compared to Fig. 7(b). While the  $\text{Ar}^*$  density continues to increase in regions farther from the plasma zone as the plasma region radius increases (similar to the trends shown at 1 mTorr), the higher background density mitigates this process by increasing the loss channel through quenching reactions with the background gas species.

An additional effect of changing the radius of the plasma region is a more uniform average incidence angle at larger radii. The average angle of incidence at a pressure of 1 mTorr for various plasma region radii is shown in Fig. 17. For the smaller radii, a minimum average angle is observed, a product of the ballistic hydrogen created in the plasma region restricted to a volume around the axis. As the radius increases, hot hydrogen atoms are created more uniformly opposite the substrate downstream, giving the uniform mean angle observed.

The flux of  $\text{SiH}_3$  and the average incidence angle for particles at 1 mTorr for various lengths of the deposition region are shown in Fig. 18. A shadowing



effect similar to that for the average incidence angle for various plasma region radii can be seen here. As the substrate is moved away from the smaller radius plasma region, more of the plasma is directly "seen" by the substrate, unimpeded by the walls of the plasma region. This allows a more uniform deposition of  $\text{SiH}_3$  particles on the substrate. Wall losses do become greater, however, leading to a reduction in the mean flux to the substrate.

## IV. DISCUSSION

The results discussed above show that the addition of the advective field leads to an increased density of various neutral radical species downstream with an accompanying increased flux to the substrate. The results also showed the effect of pressure on the densities downstream. At low-pressure,  $\text{SiH}_3$  experiences less wall loss, thus allowing a higher fraction of the molecules created in the plasma to reach the substrate. This is especially true for gas reactive species such as  $\text{SiH}_2$ . Furthermore, the ballistic transport of H atoms created hot in the plasma becomes dominant at lower pressures. The result is an increase of  $\text{SiH}_3$  density at the center of the substrate created from the hydrogen atoms undergoing extraction reactions with the surrounding silane. From an increase in pressure also comes an increase in the average angle of incidence for the radical species. At the lower pressures at which the hot atom effects were more significant, the increased flux of ballistic hydrogen atoms arriving at the substrate with relatively few collisions tends to make the average incidence angle near the center of the substrate more normal compared to the edge.

Changes in the geometry of the reactor caused changes in the densities of  $\text{SiH}_3$  and  $\text{Ar}^*$  throughout the reactor. Larger plasma region radii yield a greater flux of the radicals out of the plasma region and generally yield larger flux to the substrate. The dependence of  $\text{SiH}_3$  flux to the substrate on the length of the deposition region showed a more uniform flux across the radius of the substrate as the length increased. The average angle of incidence is more uniform at larger deposition region lengths as well.

While efforts were made to provide an accurate model for neutral radical transport in low-pressure reactors, certain approximations were made that must be addressed.

The model inputs rate coefficients for the various collisions which are independent of particle energy. For the majority of species considered and at the conditions described, this approximation is valid. However, for the increased velocity of the hydrogen atoms created in the plasma region, the rate coefficient for momentum transfer with the surrounding gas is not accurate. The model does not provide for handling rate coefficients and probabilities of collisions as a function of energy, which would be required to describe the ballistic hydrogen atoms accurately. Noting that as the velocity of a particle increases its likelihood of being forward scattered increases as well, the results given above reflect an underestimation of the effect of the hot atoms. More accurate calculations should enhance the effects described.

To determine the sensitivity of the model to the sticking coefficients used, two cases were run, doubling the values previously used for the wall sticking coefficient. The plasma region radius is 6 cm, the deposition region radius is 30 cm, and pressures of 1 mTorr and 25 mTorr were used. Figure 19(a) shows the ratio of the radially resolved flux to the substrate for  $\text{SiH}_3$  and  $\text{SiH}_2$  at 1 mTorr, normalized to those values obtained with the original sticking coefficients. A slight uniform decrease is seen for the  $\text{SiH}_3$  radical flux for the higher sticking values, while the  $\text{SiH}_2$  shows a stronger, nonuniform decrease across the radius, with the maximum effect occurring near the edge. With the doubling of the original values, the sticking coefficient for  $\text{SiH}_3$  still remains small, only 4%, whereas the  $\text{SiH}_2$  wall sticking coefficient rises to 20%, giving the greater effect on the  $\text{SiH}_2$ . For particles near the wall, the increased sticking coefficient results in smaller densities of  $\text{SiH}_3$  and  $\text{SiH}_2$  from the increased adsorption. This results in a smaller flux to the substrate edges. As the pressure is increased, the mean free path of the particles is decreased. More particles are able to reach the substrate

before being adsorbed by the wall. This accounts for the mitigated effect seen in the results at 25 mTorr shown in Fig. 19(b).

In Section II, we discussed a method whereby the thermal component of the advective flow field is accounted for during particle-fluid collisions. The degree of thermalization of the fluid element is characterized by a factor  $f$  ( $f = 1$  implies full thermalization). The density of  $\text{SiH}_3$  at 25 mTorr is shown with  $f = 0$  (collisions only with advective flow field) in Fig. 20(a) and for  $f = 0.3$  and  $f = 0.5$  in Figs. 20(b) and (c), respectively. A single pulse of particles was created in the plasma zone and allowed to transport in the advective flow field without any loss of particles to gas phase or wall reactions. Reactions at the substrate surface though were allowed. The densities are time integrated over the duration of the simulation. In the case of no added thermalization in Fig. 20(a), the particles tend to "thermalize" quickly with the background flow field and be "pushed" to regions near the substrate where the advective flow field stagnates (see Fig. 2). The particles then pool in this region, giving higher densities. This effect is not due to the ballistic hydrogen effect seen earlier since all chemical reactions are turned off. As additional thermal energy is added, the pooling of these particles ceases, and the density is more evenly distributed, as can be seen in Figs. 20(b) and (c). The flux of  $\text{SiH}_3$  molecules and H atoms to the substrate for the pulsed plasma source is shown in Fig. 21 for various degrees of thermalization of the flow field. For both species, a strong peak occurs for the case of no added thermalization. This is due to the pooling of particles in the stagnant area near the substrate. The off-center positioning of the peak is due to the radial flow of the advective field in the region approaching the substrate (see Fig. 2). Since the  $\text{SiH}_3$  mass is nearly equal to the molecular mass of the Ar and  $\text{SiH}_4$ , the transfer of momentum is more efficient for the  $\text{SiH}_3$  than for the H atoms, resulting in a larger shift of

the peak from the center of the substrate. As the fraction of added thermal energy increases, the flux becomes more uniform.

To examine the sensitivity of the choice of the amount of added thermal energy on the results, the simulation was performed on a 25 mTorr case with a quasi-continuous plasma for various fractional values of added thermal energy. The resulting flux of H atoms to the substrate is shown in Fig. 22(a). The values are normalized to the peak value for each case. It can be seen that for the continuous plasma cases, there is little change on the flux profile for the various fractions of the added thermal energy. The normalized average incident angle for these cases is shown in Fig. 22(b). While the profile for the values obtained using no added thermal energy is quite different from those values obtained with additional energy, the profiles are insensitive to the choice of added energy used in the simulation, provided  $f > 0.2 - 0.3$ .

Other conditions that were not considered were chemical reactions at the walls of the vessel where the created species are neutral radical Monte Carlo species, and the additional ability to accurately account for ions. For low-pressure discharges, Coburn<sup>10</sup> reports fractional ionization typically can be as high as  $10^{-3}$ . Shirai and Gonda<sup>29</sup> report ion densities of  $10^{10} - 10^{11} \text{ cm}^{-3}$  for a low-pressure CVD reactor operating at 0.75 mTorr. Furthermore, Tachibana<sup>37</sup> and Kushner<sup>44,45</sup> calculate ion species densities that are comparable to the radical densities. Therefore, further improvements in the model should take into account the ion transport and chemistry.

The model also assumes that any reflection of particles at the wall is diffusive, and not specular. Although this assumption may be good to first order, a more realistic model would allow a combined distribution that considers both types of reflection, dependent on the surface used for the reactor vessel walls.

## V. CONCLUSIONS

A hybrid hydrodynamic-Monte Carlo model for the transport of neutral radical species in low-pressure remote plasma CVD or ECR reactors has been developed. Analysis of the results reveals that a nonuniform flux of  $\text{SiH}_3$  to the substrate at lower pressures is partly due to hydrogen atoms created hot in the plasma region and traveling ballistically to the substrate, eventually undergoing extraction reactions to increase the  $\text{SiH}_3$  density near the substrate. Also to be noted is the higher flux rate of  $\text{SiH}_2$  to the substrate at these lower pressures coming from a lower loss rate at the lower densities of the background gas. The average angle of incidence onto the substrate from the depositing species is shown to be affected by the reactor geometry, as well as the above-mentioned hot atoms.

TABLE 1. MODEL PARAMETERS

SPECIES	WALL STICKING COEFFICIENT	SUBSTRATE STICKING COEFFICIENT	LENNARD- JONES CROSS SECTION (A)
$\text{SiH}_4$	0	0	3.84
Ar	0	0	3.44
$\text{SiH}^\dagger$	0.2	0.4	3.84
$\text{SiH}_2^\dagger$	0.1	0.32	3.84
$\text{SiH}_3^\dagger$	0.02	0.1	3.84
$\text{Si}_2\text{H}_6^\dagger$	0	0	4.42
$\text{Si}_2\text{H}_5^\dagger$	0.02	0.04	4.33
$\text{Si}_2\text{H}_4^\dagger$	0.1	0.2	4.23
$\text{H}_2^\dagger$	0	0	2.94
$\text{H}^\dagger$	0.01	0.01	2.50
$\text{Ar}^{*\dagger}$	1	1	3.44

† designates species created in plasma.

TABLE 2. REACTION SCHEME

$\text{SiH}_4 + \text{H} \rightarrow \text{SiH}_3 + \text{H}$	$2.50 \times 10^{-13}$	55
$\text{SiH}_4 + \text{SiH} \rightarrow \text{Si}_2\text{H}_5$	$2.50 \times 10^{-12}$	56,57,58
$\text{SiH}_4 + \text{SiH} \rightarrow \text{Si}_2\text{H}_3 + \text{H}_2$	$1.70 \times 10^{-12}$	56,57,58
$\text{SiH}_4 + \text{SiH}_2 \rightarrow \text{Si}_2\text{H}_6$	$4.05 \times 10^{-13}$	59,60 <sup>c</sup>
$\text{SiH}_4 + \text{SiH}_3 \rightarrow \text{Si}_2\text{H}_5 + \text{H}_2$	$1.78 \times 10^{-15}$	61
$\text{SiH}_4 + \text{Si}_2\text{H}_4 \rightarrow \text{Si}_3\text{H}_8$	$1.27 \times 10^{-12}$	60 <sup>c</sup>
$\text{SiH}_4 + \text{Si}_2\text{H}_5 \rightarrow \text{Si}_2\text{H}_6 + \text{SiH}_3$	$5.00 \times 10^{-13}$	est.
$\text{SiH}_3 + \text{H} \rightarrow \text{SiH}_2 + \text{H}_2$	$2.00 \times 10^{-11}$	55
$\text{SiH}_3 + \text{Si}_2\text{H}_5 \rightarrow \text{Si}_3\text{H}_8$	$1.00 \times 10^{-11}$	est.(62)
$\text{SiH}_3 + \text{Si}_2\text{H}_6 \rightarrow \text{SiH}_4 + \text{Si}_2\text{H}_5$	$1.00 \times 10^{-14}$	est.(55)
$\text{SiH}_2 + \text{SiH} \rightarrow \text{Si}_2\text{H}_3$	$7.22 \times 10^{-13}$	61
$\text{SiH}_2 + \text{H}_2 \rightarrow \text{SiH}_4$	$7.27 \times 10^{-13}$	63 <sup>c</sup>
$\text{SiH}_2 + \text{Si}_2\text{H}_6 \rightarrow \text{Si}_3\text{H}_8$	$1.93 \times 10^{-12}$	60,63 <sup>c</sup>
$\text{SiH} + \text{H}_2 \rightarrow \text{SiH}_3$	$1.98 \times 10^{-12}$	61
$\text{Si}_2\text{H}_6 + \text{H} \rightarrow \text{SiH}_3 + \text{SiH}_4$	$1.11 \times 10^{-12}$	64
$\text{Si}_2\text{H}_6 + \text{H} \rightarrow \text{Si}_2\text{H}_5 + \text{H}_2$	$2.16 \times 10^{-12}$	64,65
$\text{SiH}_2 + \text{SiH}_4 \rightarrow \text{Si}_2\text{H}_4 + \text{H}_2$	$1.10 \times 10^{-11}$	est.(60,63) <sup>c</sup>
$\text{SiH}_3 + \text{SiH}_3 \rightarrow \text{SiH}_2 + \text{SiH}_4$	$5.10 \times 10^{-12}$	63 <sup>c</sup>
$\text{SiH}_3 + \text{SiH}_3 \rightarrow \text{Si}_2\text{H}_4 + \text{H}_2$	$9.00 \times 10^{-13}$	63 <sup>c</sup>
$\text{Si}_2\text{H}_5 + \text{Si}_2\text{H}_5 \rightarrow \text{Si}_4\text{H}_{10}$	$1.00 \times 10^{-11}$	est.(62)
$\text{Si}_2\text{H}_4 + \text{Si}_2\text{H}_6 \rightarrow \text{Si}_4\text{H}_{10}$	$1.00 \times 10^{-11}$	est.(62)
$\text{Si}_2\text{H}_4 + \text{H}_2 \rightarrow \text{Si}_2\text{H}_6$	$5.33 \times 10^{-13}$	61
$\text{Si}_2\text{H}_4 + \text{H}_2 \rightarrow \text{SiH}_4 + \text{SiH}_2$	$3.56 \times 10^{-9}$	61



TABLE 2. (cont.)

$\text{Ar}^* + \text{H}_2 \rightarrow 2\text{H} + \text{Ar}$	$7.00 \times 10^{-11}$	66
$\text{Ar}^* + \text{SiH}_4 \rightarrow \text{SiH}_2 + 2\text{H} + \text{Ar}$	$4.56 \times 10^{-10}$	67
$\text{Ar}^* + \text{SiH}_4 \rightarrow \text{SiH} + \text{H} + \text{H}_2 + \text{Ar}$	$2.40 \times 10^{-11}$	67
$\text{Ar}^* + \text{SiH}_3 \rightarrow \text{SiH}_2 + \text{H} + \text{Ar}$	$1.00 \times 10^{-10}$	est.(66,68) <sup>a</sup>
$\text{Ar}^* + \text{SiH}_2 \rightarrow \text{SiH} + \text{H} + \text{Ar}$	$1.00 \times 10^{-10}$	est.(66,68) <sup>a</sup>
$\text{Ar}^* + \text{SiH} \rightarrow \text{Si} + \text{H} + \text{Ar}$	$1.00 \times 10^{-10}$	est.(66,68) <sup>a</sup>
$\text{Ar}^* + \text{Si}_2\text{H}_6 \rightarrow \text{Si}_2\text{H}_4 + 2\text{H} + \text{Ar}$	$6.60 \times 10^{-10}$	est.(66,68) <sup>a</sup>
$\text{Ar}^* + \text{Si}_2\text{H}_4 \rightarrow \text{Si}_2\text{H}_2 + 2\text{H} + \text{Ar}$	$6.60 \times 10^{-10}$	est.(66,68) <sup>a</sup>
$\text{SiH} + \text{Si}_2\text{H}_6 \rightarrow \text{Si}_3\text{H}_7$	$1.00 \times 10^{-11}$	est.
$\text{SiH}_2 + \text{H} \rightarrow \text{SiH} + \text{H}_2$	$7.96 \times 10^{-13}$	57
$\text{SiH}_2 + \text{H} \rightarrow \text{SiH}_3$	$1.11 \times 10^{-12}$	57
$\text{SiH}_2 + \text{SiH}_3 \rightarrow \text{Si}_2\text{H}_5$	$3.77 \times 10^{-13}$	57
$\text{SiH}_2 + \text{M} \rightarrow \text{SiH}_2 + \text{M}$	$8.91 \times 10^{-11}$	b
$\text{Si}_2\text{H}_6 + \text{M} \rightarrow \text{Si}_2\text{H}_6 + \text{M}$	$9.92 \times 10^{-11}$	b
$\text{H}_2 + \text{M} \rightarrow \text{H}_2 + \text{M}$	$1.56 \times 10^{-10}$	b
$\text{Ar}^* + \text{M} \rightarrow \text{Ar}^* + \text{M}$	$6.63 \times 10^{-11}$	b
$\text{H} + \text{M} \rightarrow \text{H} + \text{M}$	$1.58 \times 10^{-10}$	b
$\text{Si}_2\text{H}_4 + \text{M} \rightarrow \text{Si}_2\text{H}_4 + \text{M}$	$9.14 \times 10^{-11}$	b
$\text{SiH} + \text{M} \rightarrow \text{SiH} + \text{M}$	$9.00 \times 10^{-11}$	b
$\text{SiH}_3 + \text{M} \rightarrow \text{SiH}_3 + \text{M}$	$8.83 \times 10^{-11}$	b
$\text{Si}_2\text{H}_5 + \text{M} \rightarrow \text{Si}_2\text{H}_5 + \text{M}$	$9.55 \times 10^{-11}$	b

a) Rate constant estimated by analogy to  $\text{CH}_4$ ,  $\text{C}_2\text{H}_6$ , and their radicals.

b) Rate constant calculated using Lennard-Jones parameters and formula as given in text.

c) Value listed is computed for 10 mTorr.

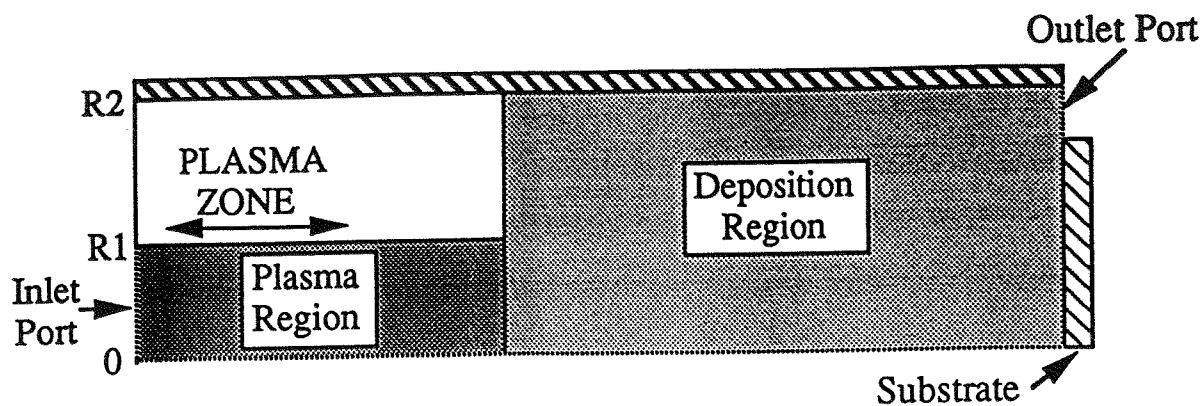


Figure 1. Schematic of the model reactor with regions referred to in text.

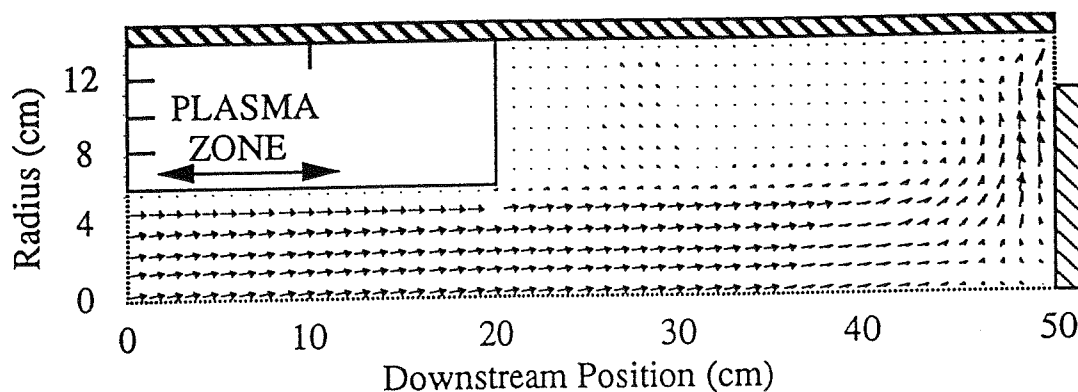


Figure 2. The advective flow field for a 6 cm radius plasma region, 30 cm long deposition region. The arrow lengths range over a linear scale.

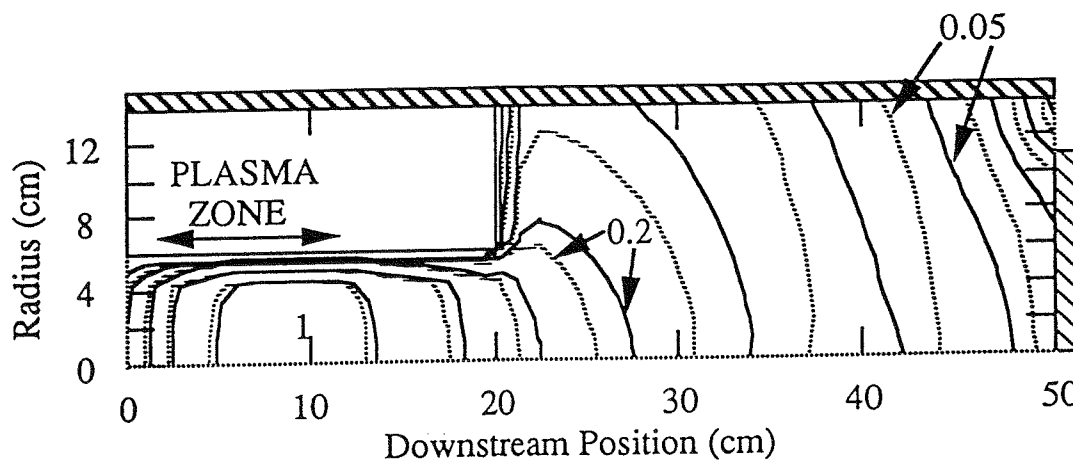


Figure 3.  $\text{SiH}_3$  density for a pressure of 25 mTorr. The solid lines indicate density contours for a case using a flowing background gas, while the broken lines indicate the case of a static gas.

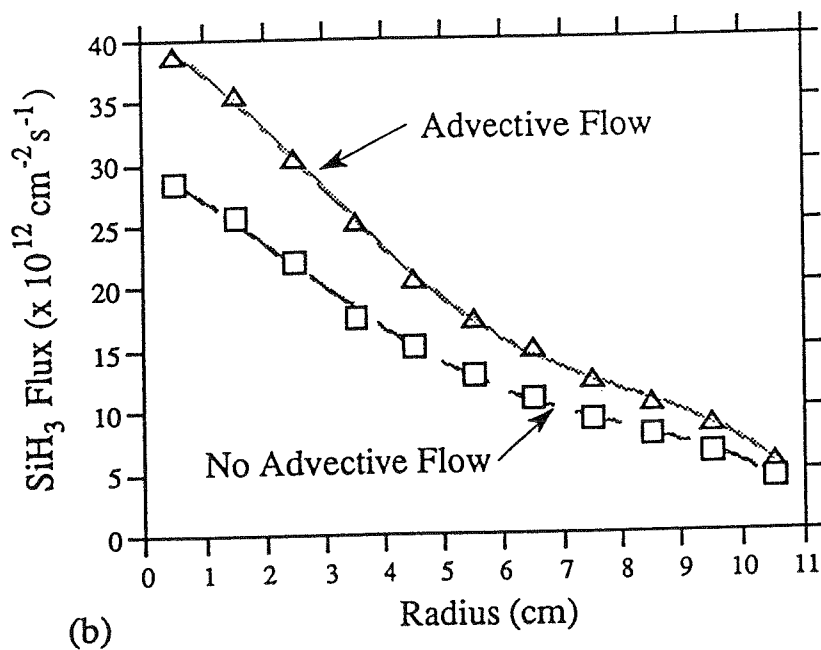
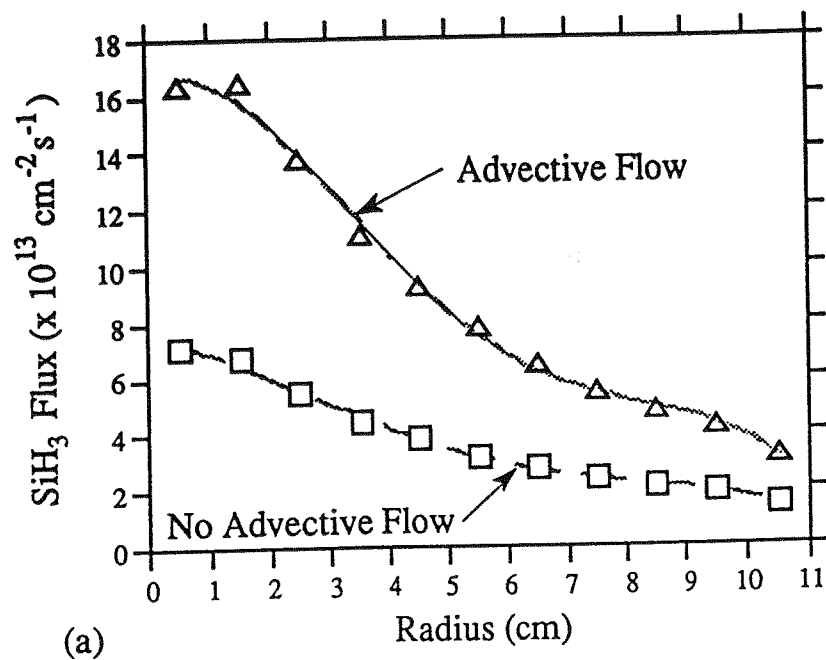


Figure 4.  $\text{SiH}_3$  flux to the substrate comparing a flowing vs. static background gas, for (a) 1 mTorr and (b) 25 mTorr.

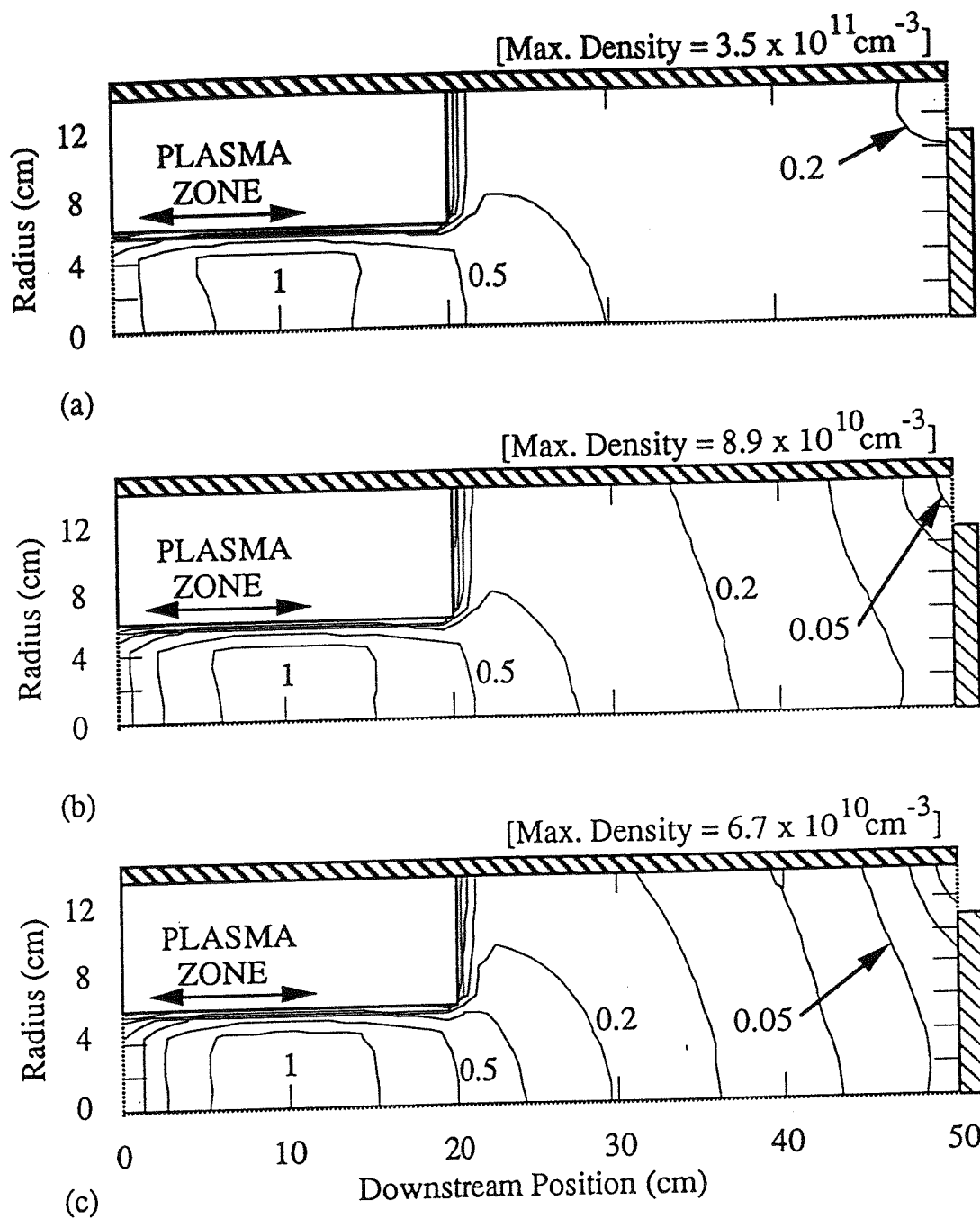


Figure 5.  $\text{SiH}_3$  density for (a) 1 mTorr, (b) 10 mTorr, and (c) 25 mTorr. Larger gradients occur at the higher pressures from increased wall losses.

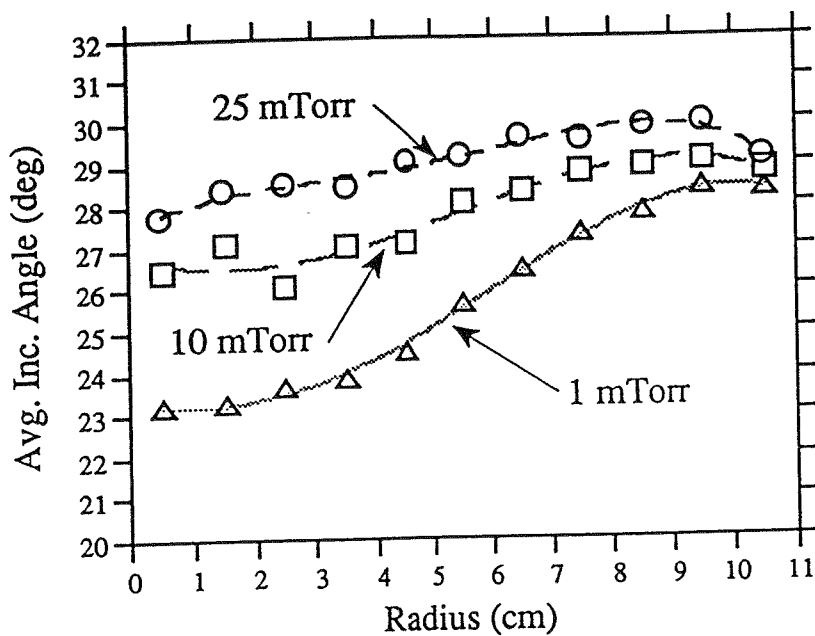


Figure 6. The average incidence angle (from normal) for particle flux to the substrate at various pressures. Nonuniformity of values at lower pressures come from hot atom effects (see text).

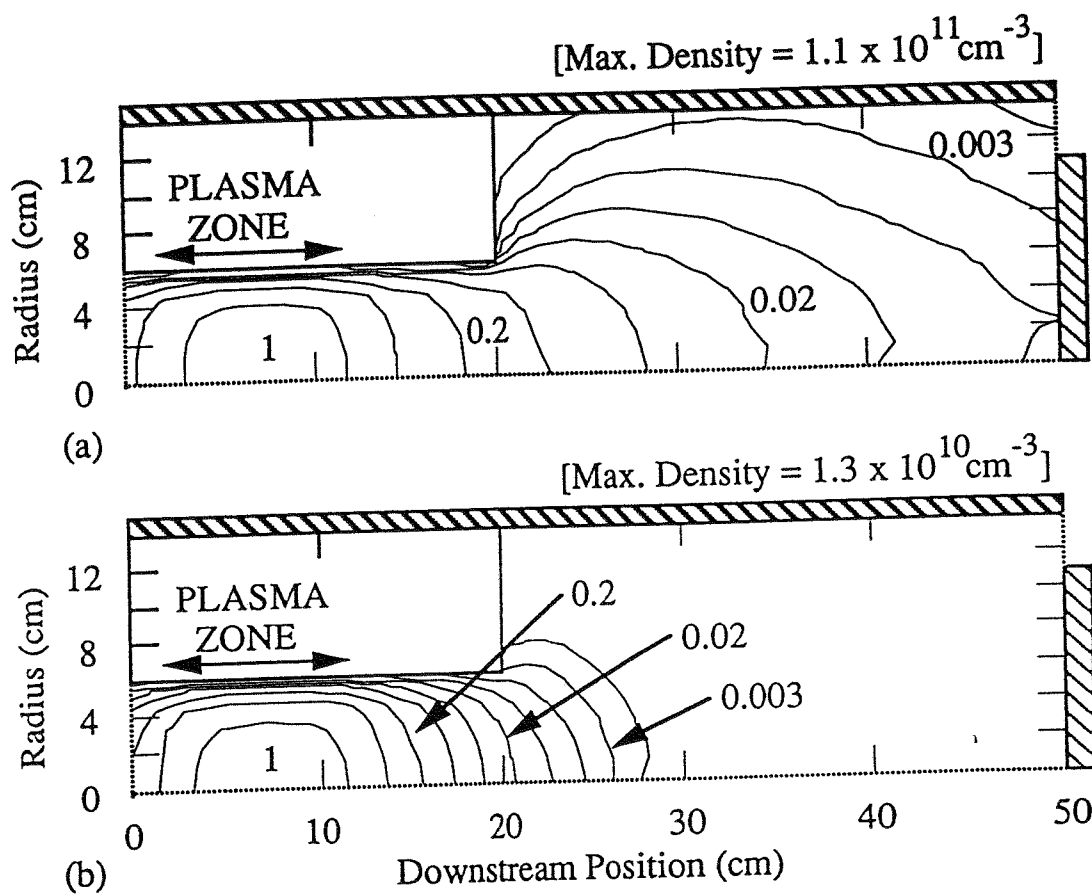


Figure 7.  $\text{Ar}^*$  density at (a) 1 mTorr and (b) 25 mTorr. Larger density gradients in (b) are due to increased quenching by gas collisions.

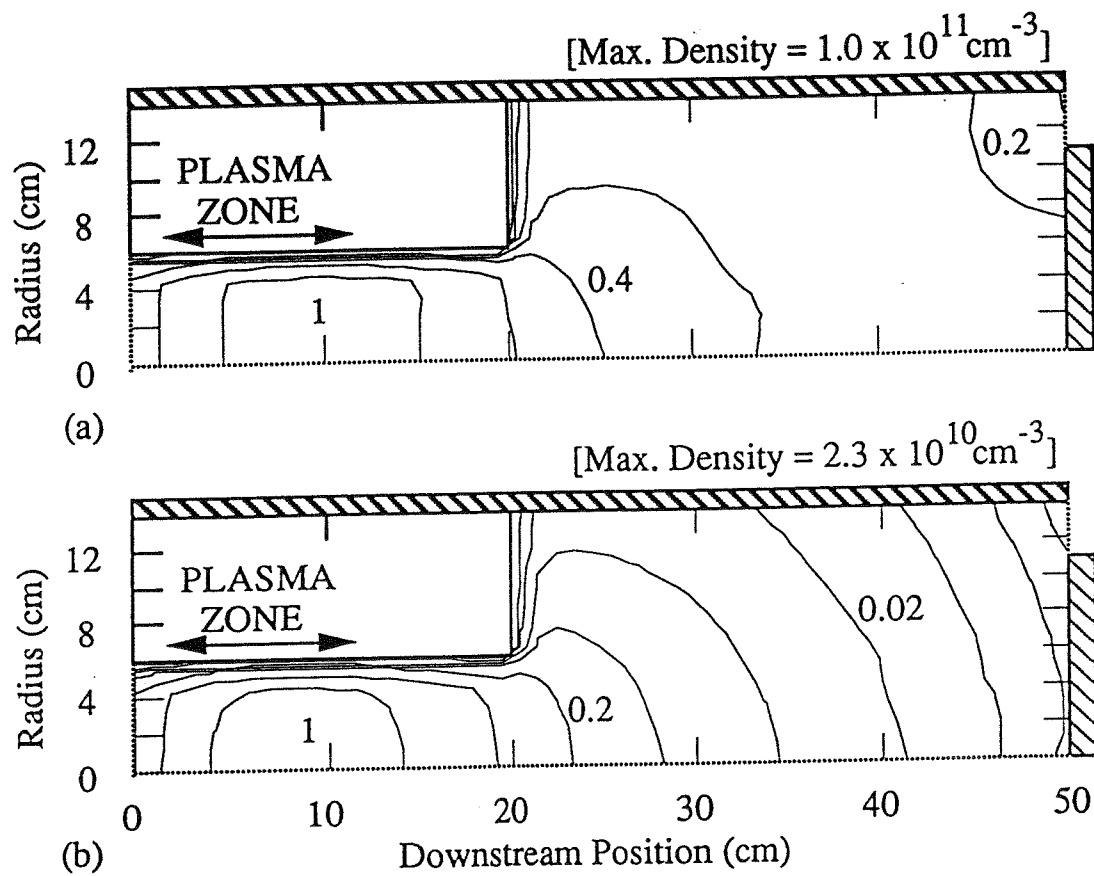


Figure 8.  $\text{SiH}_2$  density at (a) 1 mTorr and (b) 25 mTorr.

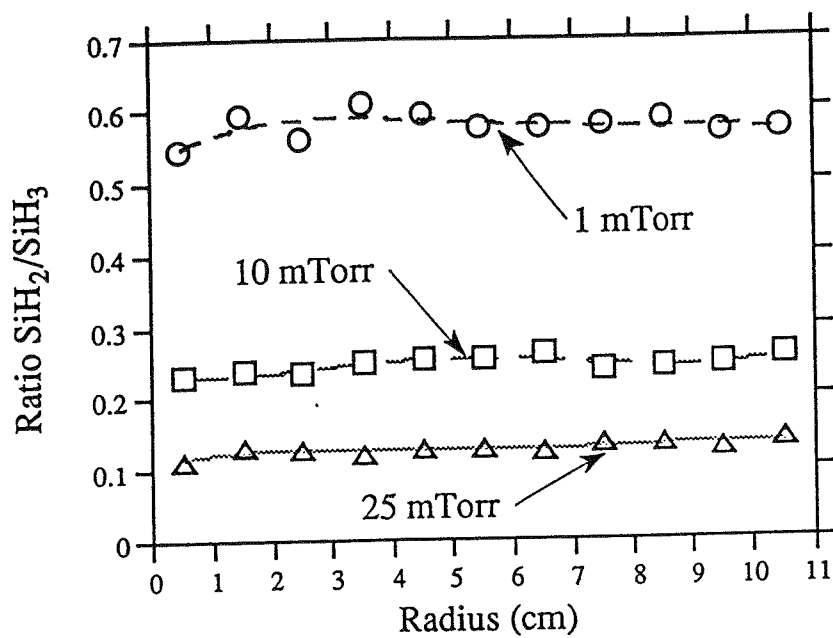


Figure 9. Ratio of  $\text{SiH}_2$  flux/ $\text{SiH}_3$  flux to the substrate at various pressures. The increased gas and wall losses at the higher pressures lead to smaller fractions of  $\text{SiH}_2$  depositing onto the substrate.



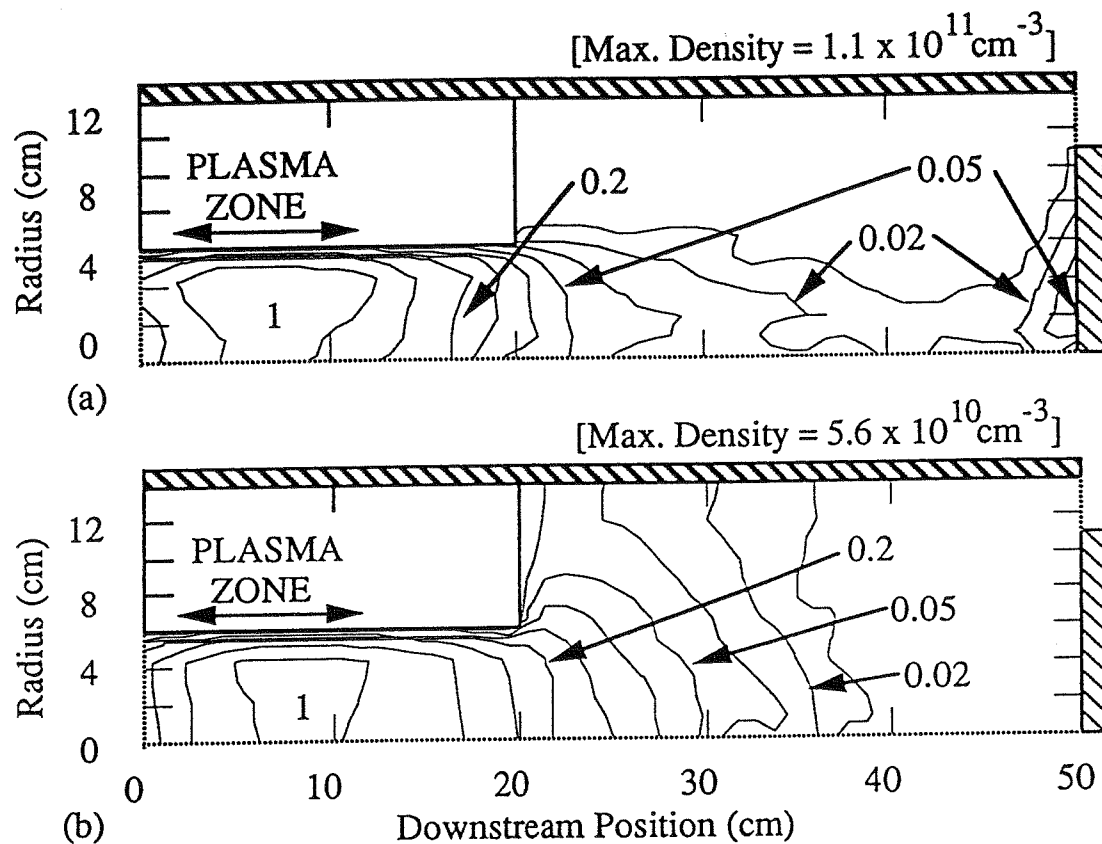


Figure 10.  $\text{SiH}_3$  density for (a) 1 mTorr and (b) 10 mTorr, at a time after plasma turn on of 0.3 ms and 3 ms, respectively. A local maximum can be seen at the substrate in (a) coming from H atoms created hot in the plasma and ballistically traveling to the substrate, where they eventually undergo extraction reactions to yield increased densities of  $\text{SiH}_3$ .

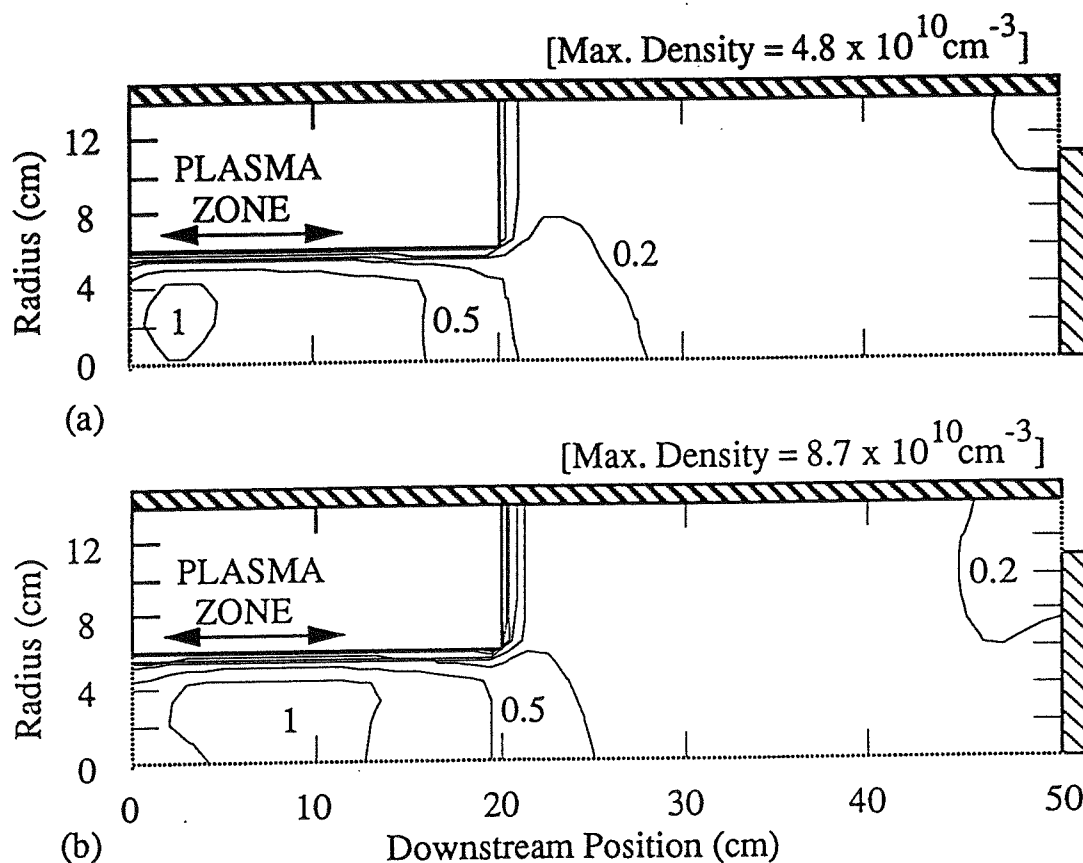


Figure 11. H atom density for 1 mTorr case. H atoms in (a) are the product of  $\text{SiH}_4$  dissociation to  $\text{SiH}_2$  and  $2\text{H}$ , and H atoms in (b) come from the dissociation to  $\text{SiH}_3$  and H. The higher density at the substrate in (b) gives the source of thermalized H atoms, leading to higher  $\text{SiH}_3$  densities near the substrate.

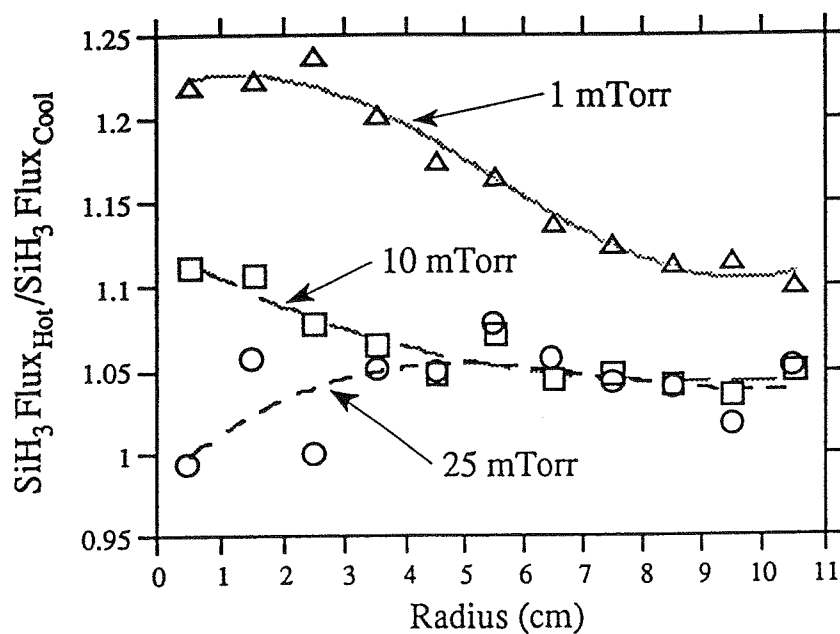


Figure 12. Ratio of  $\text{SiH}_3$  flux to the substrate for particles created with 2 eV kinetic energy in the plasma, over the  $\text{SiH}_3$  flux with particles created at the gas temperature, for various pressures. Enhancements occur predominantly at lower pressures near the center of the substrate.

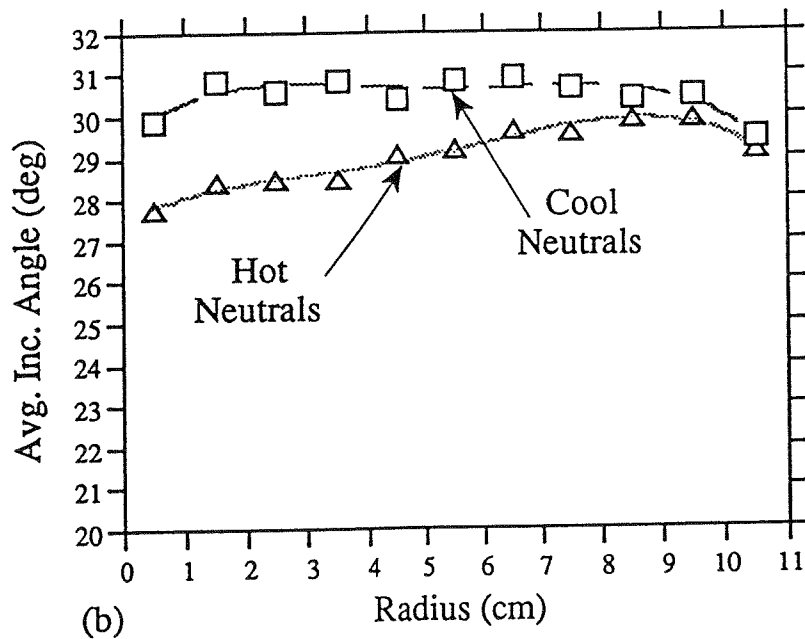
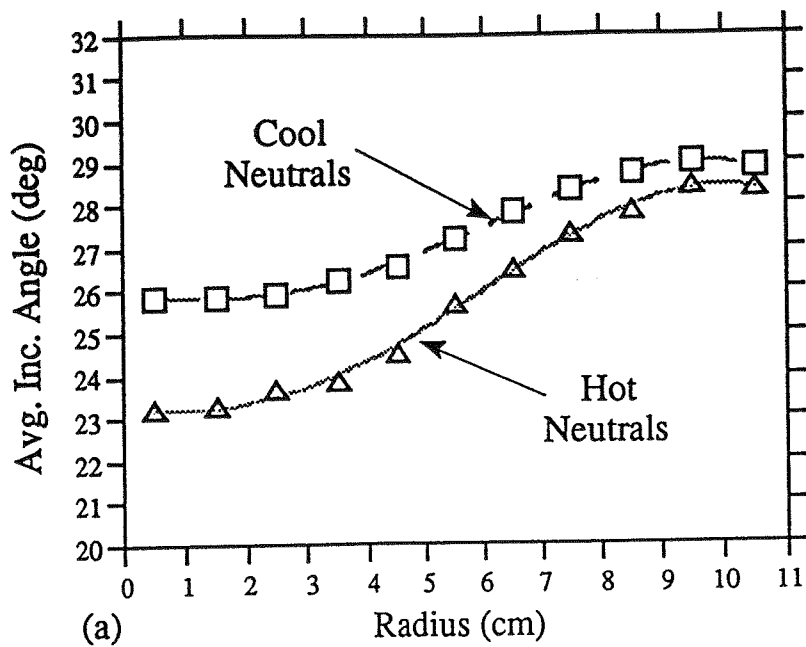


Figure 13. Average incidence angle for plasma particles created hot compared to particles created cool, at (a) 1 mTorr and (b) 25 mTorr. More normal incidence for the hot atom cases comes from ballistic transport of H atoms.

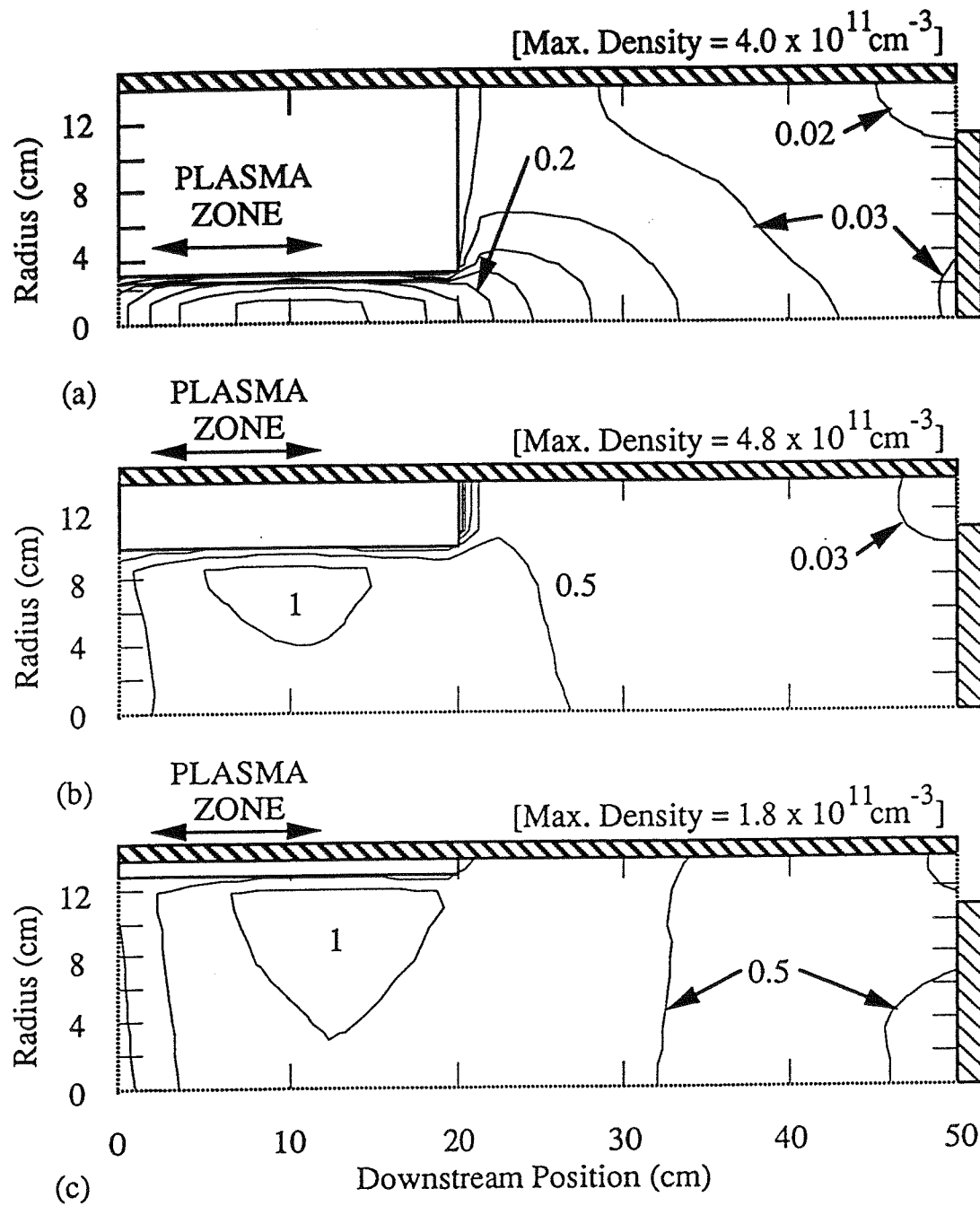


Figure 14.  $\text{SiH}_3$  density at 1 mTorr for plasma region radii of (a) 3 cm, (b) 10 cm, and (c) 13 cm.

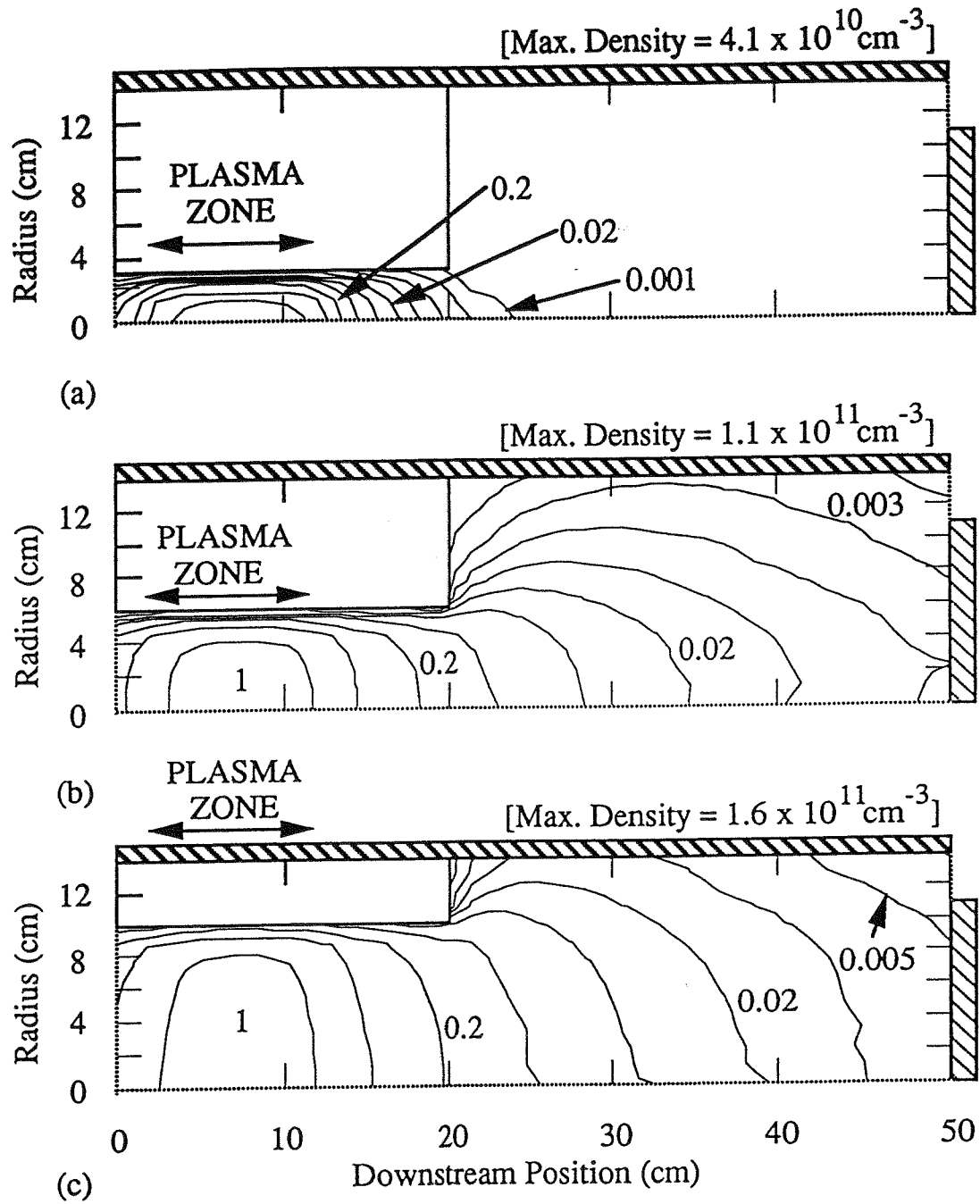


Figure 15.  $\text{Ar}^*$  density at 1 mTorr for plasma region radii of (a) 3 cm, (b) 6 cm, and (c) 10 cm. At 6 cm, the fraction of  $\text{Ar}^*$  that reaches the substrate is greater than that found for the 3 cm and 10 cm cases.

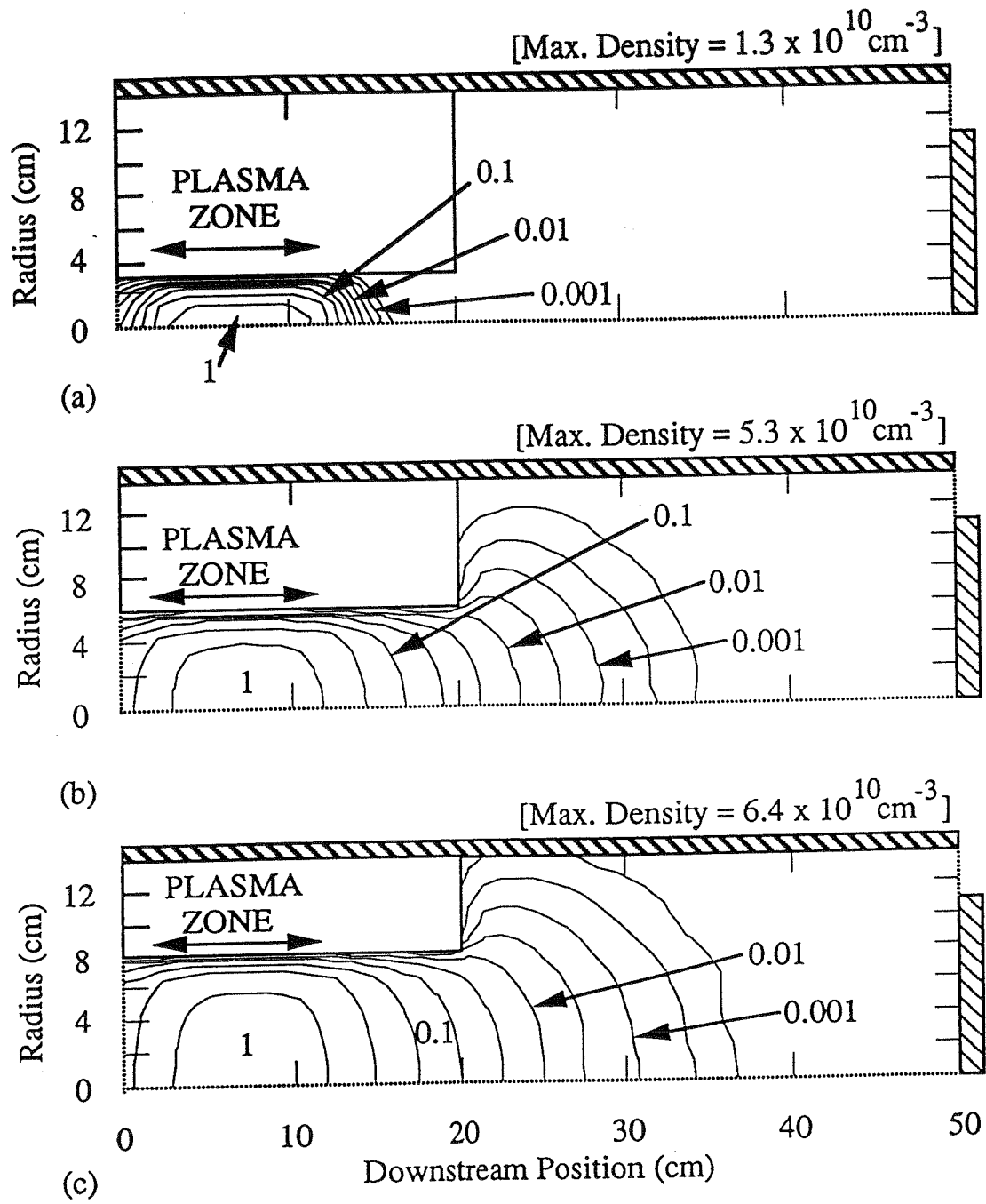


Figure 16.  $\text{Ar}^*$  density at 25 mTorr for plasma region radii of (a) 3 cm, (b) 6 cm, and (c) 8 cm. As the radius increases, wall losses decrease and the  $\text{Ar}^*$  density moves further downstream.

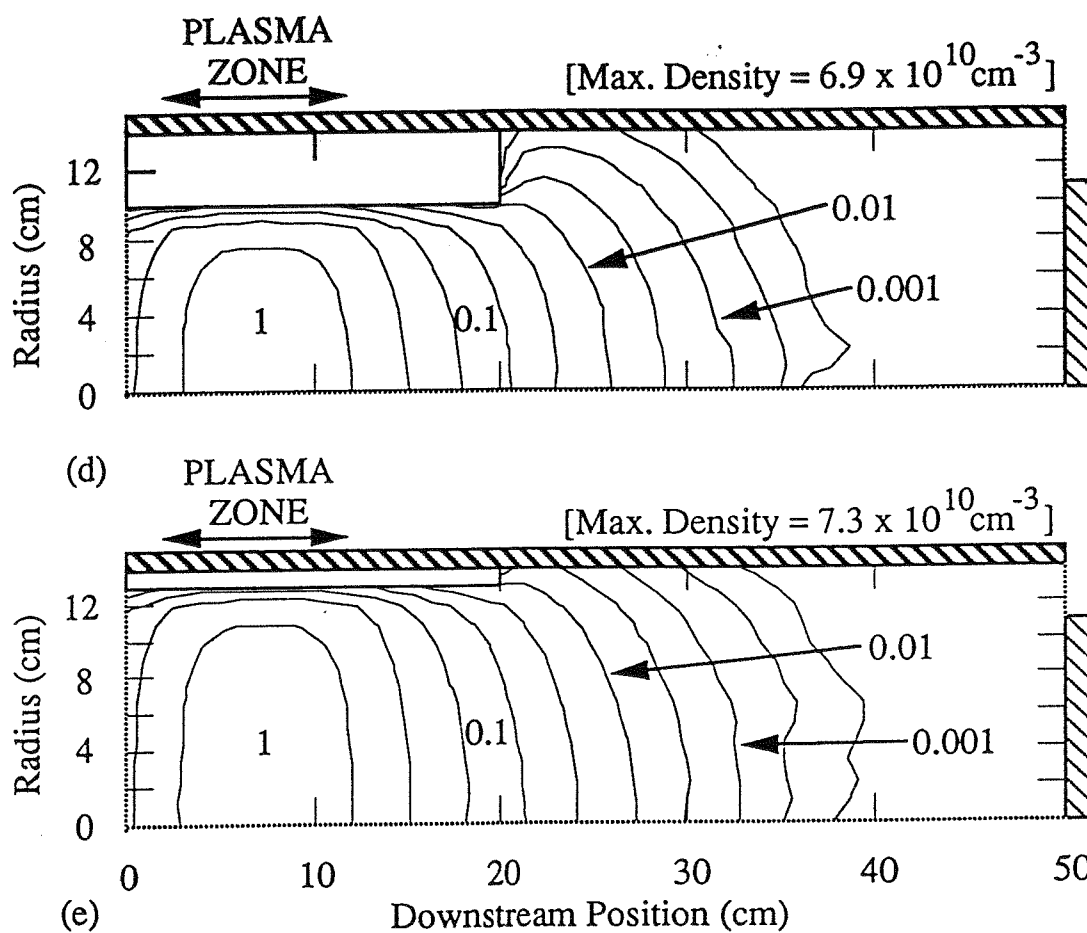


Figure 16 (cont.).  $\text{Ar}^*$  density at 25 mTorr for plasma region radii of (d) 10 cm, and (e) 13 cm.



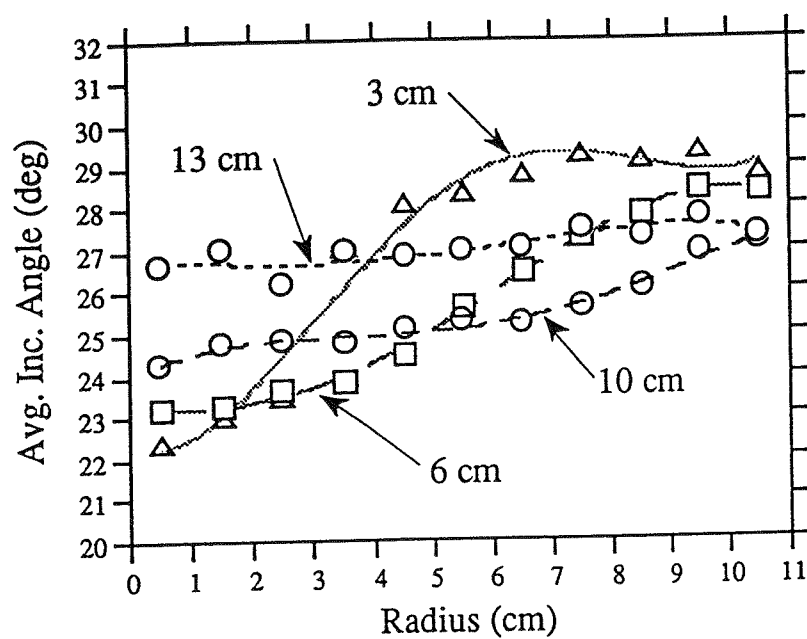
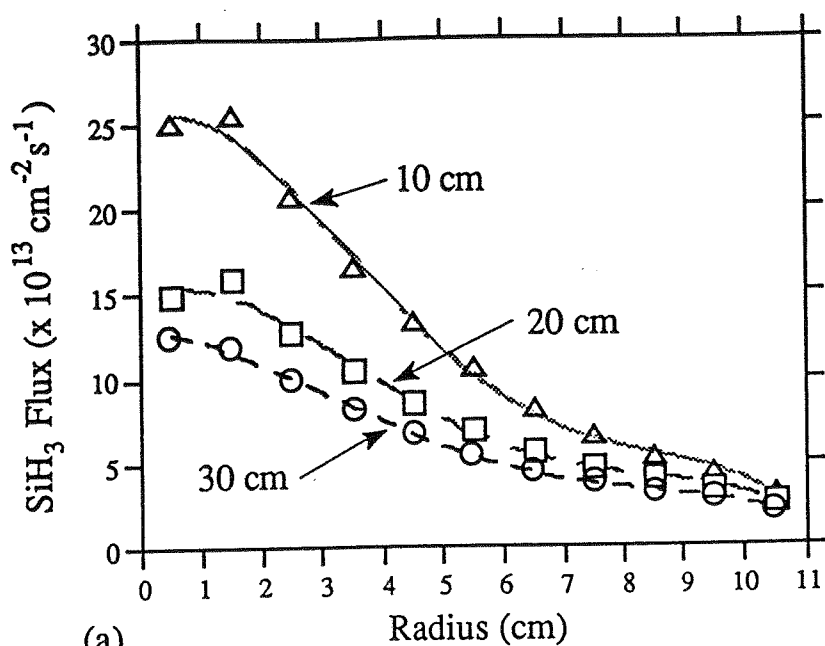
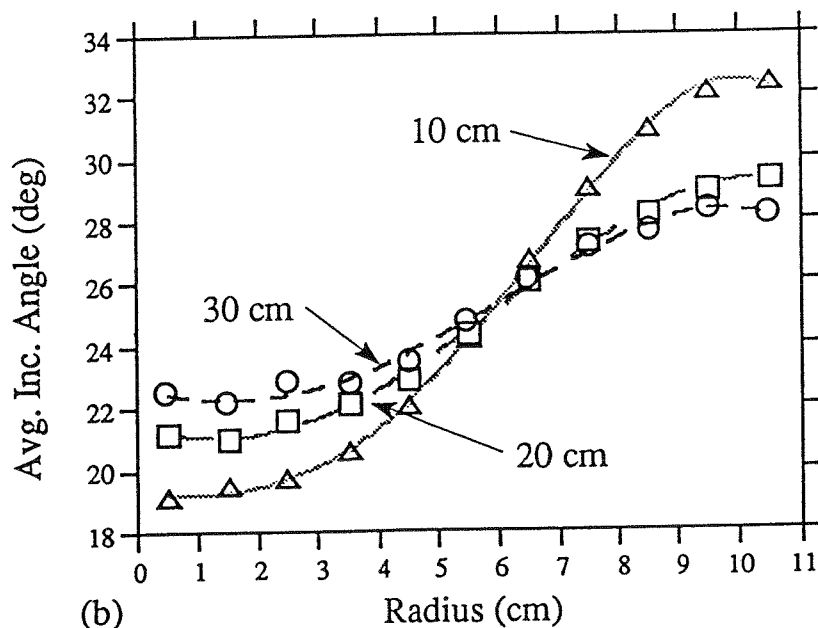


Figure 17. Average incidence angles of the substrate for various radii of the plasma region. The values become more uniform across the radius as the plasma region radius becomes comparable to the substrate radius.



(a)



(b)

Figure 18. SiH<sub>3</sub> flux to the substrate (a) and the average incidence angle for all particles (b) for various deposition region lengths. The pressure is 1 mTorr and the plasma region radius is 6 cm. Flux values and incidence angles become more uniform at longer lengths.

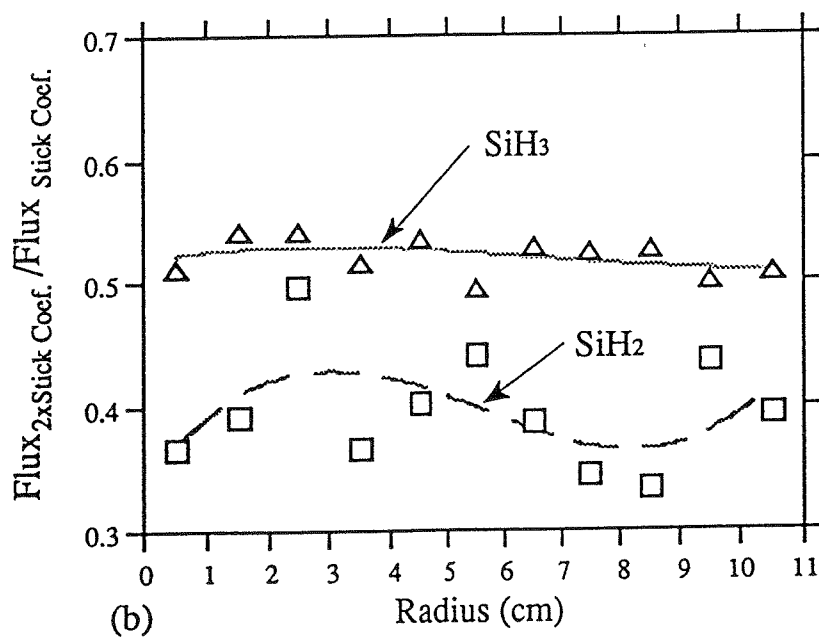
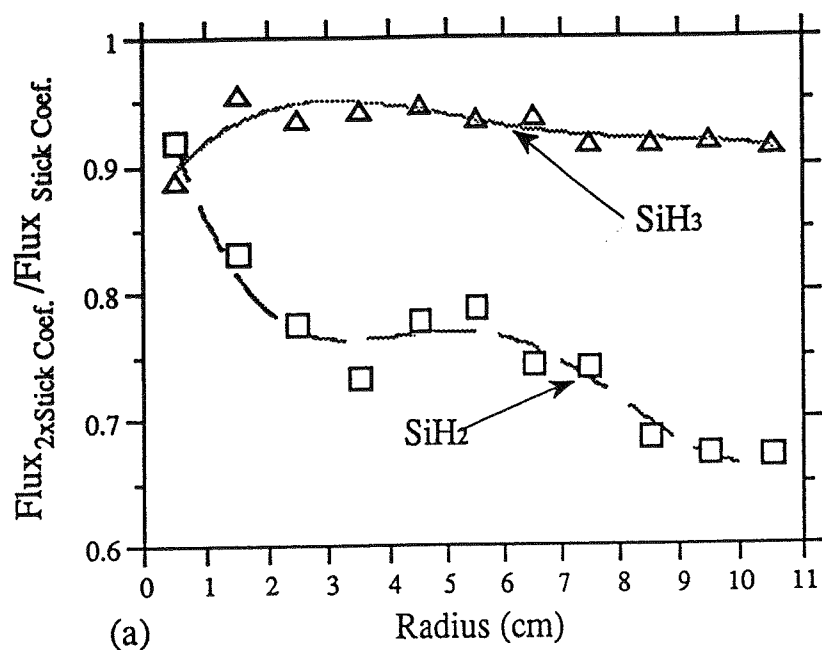


Figure 19. Ratio of particle flux calculated using sticking coefficients double their standard values to the flux calculated using the standard values, for  $\text{SiH}_2$  and  $\text{SiH}_3$ . The pressure is 1 mTorr and 25 mTorr for (a) and (b), respectively.

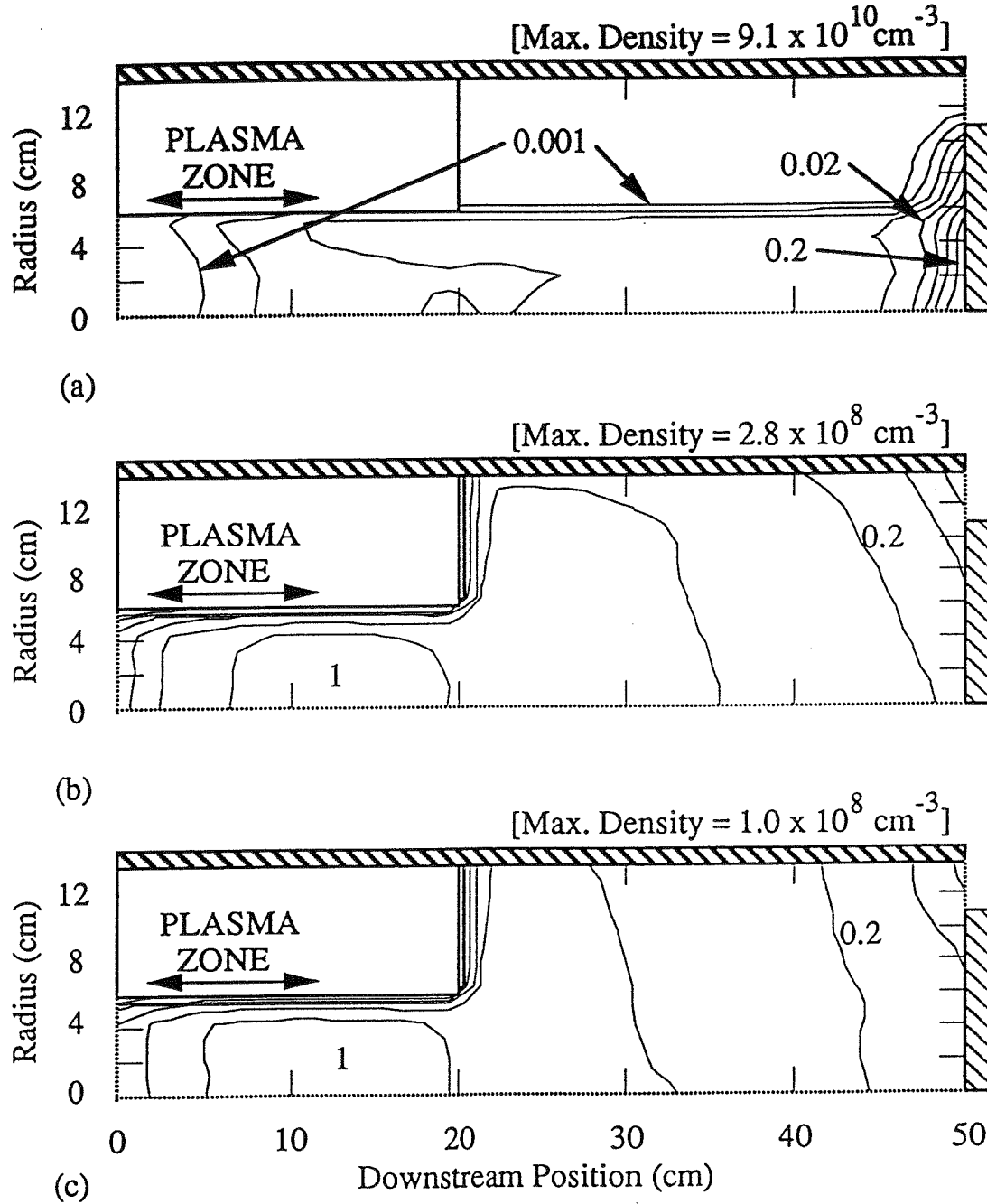
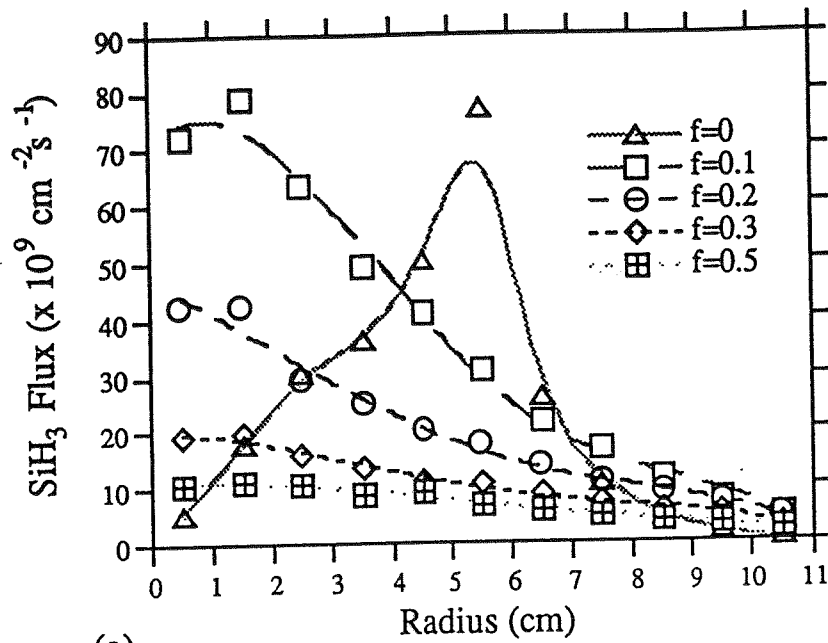
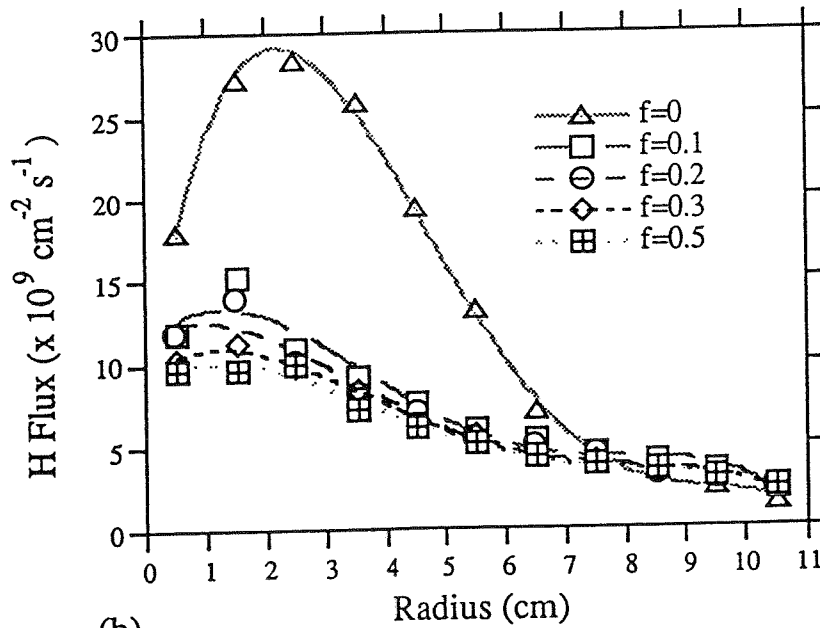


Figure 20. Time integrated  $\text{SiH}_3$  density for a single pulse plasma after 4 ms. Thermal factors for the fluid elements are (a) 0, (b) 0.3, and (c) 0.5. Maximum density in (a) occurs at the substrate where the particles pool due to stagnation of the advective. Higher multiplication factors allow particles to transport out of stagnation areas.



(a)



(b)

Figure 21. Flux of (a) SiH<sub>3</sub> and (b) H to the substrate for various added fractions of thermal energy during momentum transfer collisions with the advective flow field. The gas pressure is 25 mTorr and the plasma is pulsed once. The peak occurring for no added thermal energy results from the pooling of particles in a stagnant region of the advective flow field near the substrate.

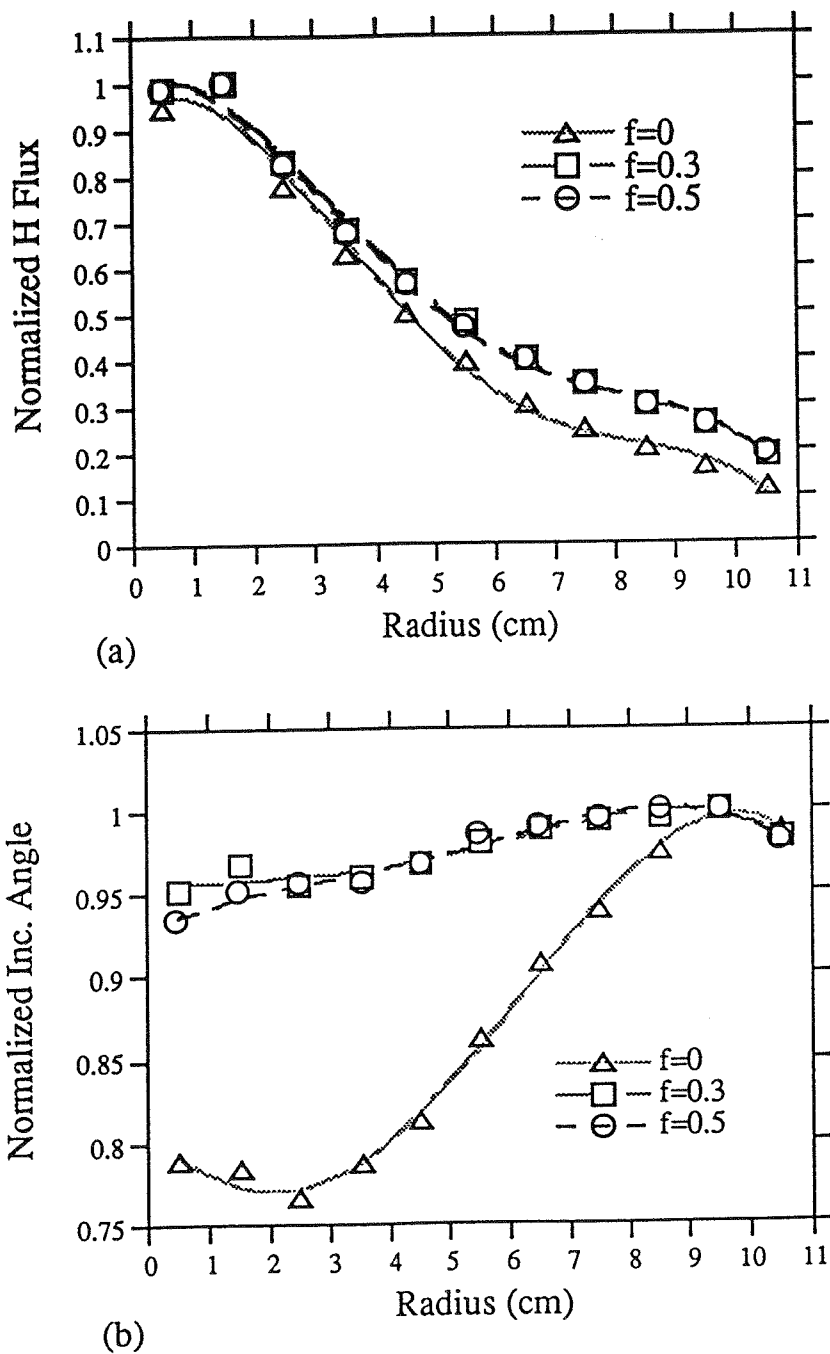


Figure 22. The (a) normalized H flux to the substrate, and the (b) normalized incident angle for various fractions of added thermal energy during momentum transfer collisions. The gas pressure is 25 mTorr and the plasma is quasi-continuous.

## REFERENCES

- <sup>1</sup>T. Hsu, R. Qian, D. Kinosky, J. Irby, B. Anthony, S. Banerjee, and A. Tasch, Spring 1991 MRS Meeting.
- <sup>2</sup>S.V. Hattangady, J.B. Psotthill, G.G. Fountain, R.A. Rudder, M.J. Mantini, and R.J. Markunas, Appl. Phys. Lett. 59, 339 (1991).
- <sup>3</sup>L. Breaux, B. Anthony, T. Hsu, S. Banerjee, and A. Tasch, Appl. Phys. Lett. 55, 1885 (1989).
- <sup>4</sup>S.V. Hattangady, R.A. Rudder, M.J. Mantini, G.G. Fountain, J.B. Posthill, and R.J. Markunas, J. Appl. Phys. 68, 1233 (1990).
- <sup>5</sup>T. Hsu, B. Anthony, R. Qian, J. Irby, S. Banerjee, A. Tasch, S. Lin, H. Marcus, and C. Magee, J. Elect. Mat. 20, 279 (1991).
- <sup>6</sup>M. Delfino, S. Salimian, D. Hodul, J. Appl. Phys. 70, 1712 (1991).
- <sup>7</sup>K. Fukuda, J. Murota, S. Ono, T. Matsuura, H. Uetake, and T. Ohmi, Appl. Phys. Lett. 59, 2853 (1991).
- <sup>8</sup>R. Reifand and W. Kern, in Thin Film Processes II, edited by J. Vossen and W. Kern (Academic Press, San Diego, 1991), pp. 525 - 564.
- <sup>9</sup>S. Veprek, Thin Solid Films 175, 129 (1989).
- <sup>10</sup>J.W. Coburn, IEEE Trans. Plasma Sci. 19, 1048 (1991).
- <sup>11</sup>R.F. Bunshah, IEEE Trans. Plasma Sci. 18, 846 (1990).
- <sup>12</sup>G. Lucovsky, P.D. Richard, D.V. Tsu, S.Y. Lin, and R.J. Markunas, J. Vac. Sci. Technol. A 4, 681 (1986).
- <sup>13</sup>G. Lucovsky, D.V. Tsu, G.N. Parsons, in Deposition Growth: Limits for Microelectronics, edited by G.W. Rubloff (American Inst. of Physics Conf. Proc. No. 167, New York, 1988), pp. 156 - 172.
- <sup>14</sup>D.V. Tsu, G.N. Parsons, G. Lucovsky, J. Vac. Sci. Technol. A 6, 1849 (1988).
- <sup>15</sup>G. Lucovsky and D.V. Tsu, J. Cryst. Growth 86, 804 (1988).
- <sup>16</sup>G. Lucovsky, D.V. Tsu, S.S. Kim, R.J. Markunas, and G.G. Fountain, Appl. Surf. Sci. 39, 33 (1989).

- <sup>17</sup>D.V. Tsu, G.N. Parsons, G. Lucovsky, and M.W. Watkins, J. Vac. Sci. Technol. A 7, 1115 (1989).
- <sup>18</sup>J.A. Theil, D.V. Tsu, and G. Lucovsky, J. Electron. Mat. 19, 209 (1990).
- <sup>19</sup>G. Lucovsky, D.V. Tsu, R.A. Rudder, and R.J. Markunas, in Thin Film Processes II, edited by J. Vossen and W. Kern (Academic Press, San Diego, 1991), pp. 565 - 619, and references therein.
- <sup>20</sup>S.V. Hattangady, G.G. Fountain, R.A. Rudder, and R.J. Markunas, J. Vac. Sci. Technol. A 7, 570 (1989).
- <sup>21</sup>N. Selamoglu, J.A. Mucha, D.E. Ibbotson, and D.L. Flamm, Vac. Sci. Technol. B 7, 1345 (1989).
- <sup>22</sup>J.L. Jauberteau, D. Conte, M.I. Baraton, P. Quintard, J. Aubreton, and A. Catherinot, Plasma Chem. Plasma Process. 10, 401 (1990).
- <sup>23</sup>B. Anthony, T. Hsu, L. Breaux, R. Qian, S. Banerjee, and A. Tasch, J. Electron Mat. 19, 1089 (1990).
- <sup>24</sup>B. Anthony, T. Hsu, R. Qian, J. Irby, S. Banerjee, and A. Tasch, J. Electron Mat. 20, 309 (1991).
- <sup>25</sup>K. Tanaka and A. Matsuda, Mat. Sci. Reports 2, 139 (1987).
- <sup>26</sup>P.K. Shufflebotham, D.J. Thomson, and H.C. Card, J. Appl. Phys. 64, 4398 (1988).
- <sup>27</sup>J. Forster and W. Holber, J. Vac. Sci. Technol. A 7, 899 (1989).
- <sup>28</sup>J.S. McKillop, J.C. Forster, W.M. Holber, J. Vac. Sci. Technol. A 7, 908 (1989).
- <sup>29</sup>K. Shirai and S. Gonda, J. Appl. Phys. 67, 6281 (1990).
- <sup>30</sup>J. Hopwood, D.K. Reinhard, J. Asmussen, J. Vac. Sci. Technol. A 8, 3103 (1990).
- <sup>31</sup>Y. Nakayama, M. Kondoh, K. Hitsuishii, M. Zhang and T. Kawamura, Appl. Phys. Lett. 57, 2297 (1990).
- <sup>32</sup>S. Iizuka and N. Sato, J. Appl. Phys. 70, 4165 (1991).
- <sup>33</sup>S.R. Meja, R.D. McLeod, W. Pries, P. Shufflebotham, D.J. Thomas, J. White, J. Shellenberg, K.C. Kao, and H.C. Card, J. Non-Cryst. Solids,



- 77 & 78, 765 (1985).
- <sup>34</sup>J. Hopwood and J. Asmussen, Appl. Phys. Lett. 58, 2473 (1991).
  - <sup>35</sup>I. Chen, Thin Solid Films 101, 41 (1983).
  - <sup>36</sup>A. Gallagher, J. Appl. Phys. 63, 2406 (1988).
  - <sup>37</sup>K. Tachibana, Proc. 8th Symp. on ISIAT '84, Toyko (1984), pp. 319 - 326.
  - <sup>38</sup>Y. Yamaguchi, A. Sumiyama, R. Hattori, Y. Morokuma, and T. Makabe, J. Phys. D: Appl. Phys. 22, 505 (1989).
  - <sup>39</sup>J. Perrin and T. Broekhuizen, Appl. Phys. Lett. 50, 433 (1987).
  - <sup>40</sup>S. Kalidindi, S. Desu, J. Electrochem. Soc. 137, 624 (1990).
  - <sup>41</sup>A. Rhallabi and Y. Catherine, IEEE Trans. Plasma Sci. 19, 270 (1990).
  - <sup>42</sup>D.J. Koch and W.N.G. Hitchon, J. Appl. Phys. 70, 4139 (1991).
  - <sup>43</sup>A. Garscadden, Mat. Res. Soc. Symp. Proc. 68, 127 (1986).
  - <sup>44</sup>M.J. Kushner, J. Appl. Phys. 63, 2532 (1988).
  - <sup>45</sup>M.J. Kushner, J. Appl. Phys. 71, 4173 (1992).
  - <sup>46</sup>N. Sato and H. Tagashira, IEEE Trans. Plasma Sci. 19, 102 (1991).
  - <sup>47</sup>T.J. Sommerer and M.J. Kushner, J. Appl. Phys. 71, 1654 (1992).
  - <sup>48</sup>R.K. Porteus and D.B. Graves, IEEE Trans. Plasma Sci. 19, 204 (1991).
  - <sup>49</sup>T.J. Sommerer and M.J. Kushner, J. Appl. Phys. 70, 1240 (1991).
  - <sup>50</sup>D.A. Anderson, J.C. Tannehill, and R.H. Pletcher, Computational Fluid Mechanics and Heat Transfer, (McGraw-Hill, New York, 1984), p. 199.
  - <sup>51</sup>S.L. Lin and J.N. Bardsley, J. Chem. Phys. 66, 435 (1977).
  - <sup>52</sup>M. Brennan, IEEE Trans. Plasma Sci. 19, 256 (1991).
  - <sup>53</sup>J.B. Marion, Classical Dynamics of Particles and Systems, (Academic Press, New York, 1970), p. 300.

- <sup>54</sup>J.O. Hirschfelder, C.F. Curtiss, and R.B. Bird, Molecular Theory of Gases and Liquids, (Wiley, New York, 1954), p. 529.
- <sup>55</sup>S.K. Loh and J.M. Jasinski, J. Chem. Phys. **95**, 4914 (1991).
- <sup>56</sup>J.P.M. Schmitt, P. Gressier, M. Krishnan, G. DeRosny, and J. Perrin, Chem. Phys. **84**, 281 (1984).
- <sup>57</sup>M.E. Coltrin, R.J. Kee, and J.A. Miller, J. Electrochem. Soc. **133**, 1206 (1986).
- <sup>58</sup>F.J. Kampas, J. Appl. Phys. **57**, 2290 (1985).
- <sup>59</sup>S. Koda, S. Suga, S. Tsuchuja, T. Suzuki, C. Yamada, and E. Hirota, Chem. Phys. Lett. **161**, 35 (1989).
- <sup>60</sup>D.B. Beach and J.M. Jasinski, J. Phys. Chem. **94**, 3619 (1990).
- <sup>61</sup>M.E. Coltrin, R.J. Kee, and J.A. Miller, J. Electrochem. Soc. **131**, 425 (1984).
- <sup>62</sup>P. John and J. Purnell, J. Chem. Soc. Faraday Trans. 1 **69**, 1455 (1973).
- <sup>63</sup>J.M. Jasinski and J.O. Chu, J. Chem. Phys. **88**, 1678 (1988).
- <sup>64</sup>T.L. Pollock, H.S. Sandhu, A. Jodhan, and O.P. Strausz, J. Am. Chem. Soc. **95**, 1017 (1973).
- <sup>65</sup>P.E. Vanier, F.J. Kampas, R.R. Cordermann, and G. Rajeswaran, J. Appl. Phys. **56**, 1812 (1984).
- <sup>66</sup>L.G. Piper, J.E. Velazco, and D.W. Setser, J. Chem. Phys. **59**, 3323 (1973).
- <sup>67</sup>M. Tsuji, K. Kobayashi, S. Yamaguchi, H. Obase, K. Yamaguchi, and Y. Nishimura, Chem. Phys. Lett. **155**, 481 (1989).
- <sup>68</sup>J.E. Velazco, J.H. Kolz, and D.W. Setser, J. Chem. Phys. **69**, 4357 (1978).
- <sup>69</sup>J. Perrin and T. Broekhuizen, Appl. Phys. Lett. **50**, 433 (1987).
- <sup>70</sup>T. Grotjohn, private communication.
- <sup>71</sup>S.M. Rosnagel, J. Vac. Sci. Technol. A **6**, 3049 (1988).

## VITA

Michael Joseph Hartig was born and raised in Chicago. After graduation from high school in 1979, he went to work for a local steel warehouse while attending college part time at Daley College, one of the City Colleges of Chicago. In 1983, he moved to Urbana, IL, where he continued his undergraduate studies in Electrical Engineering at the University of Illinois. He received his B.S degree in 1986.

Immediately thereafter, he continued with his graduate studies in the department of Electrical and Computer Engineering under the direction of Professor J. Gary Eden performing investigations into laser processes of various gas laser systems. He received his M.S. in 1989 with the thesis titled, "Excited State Emission and Absorption Spectra of Dikrypton Fluoride." He continued his graduate studies for the doctoral degree under the direction of Professor Mark Kushner. During his stay, he performed radially resolved electron energy calculations in low-pressure plasmas, with the results being presented at two conferences and a forthcoming paper. His current research is in the computer modeling of the transport of neutral radical and excited state species occurring in semiconductor processing reactors at intermediate pressures.

Mr. Hartig is a member of Tau Beta Pi, Eta Kappa Nu, IEEE, and the American Physical Society.